

Summary of the results from the lunar orbiter laser altimeter after seven years in lunar orbit



David E. Smith^{a,*}, Maria T. Zuber^a, Gregory A. Neumann^b, Erwan Mazarico^b, Frank G. Lemoine^b, James W. Head III^c, Paul G. Lucey^d, Oded Aharonson^e, Mark S. Robinson^f, Xiaoli Sun^b, Mark H. Torrence^g, Michael K. Barker^h, Juergen Oberst^{ij}, Thomas C. Duxbury^k, Dandan Mao^h, Olivier S. Barnouin^l, Kopal Jha^h, David D. Rowlands^b, Sander Goossens^m, David Baker^b, Sven Bauerⁱ, Philipp Gläser^j, Myriam Lemelin^d, Margaret Rosenburgⁿ, Michael M. Sori^{a,o}, Jennifer Whitten^p, Timothy Mcclanahan^b

^a Department of Earth, Atmospheric and Planetary Sciences, Massachusetts Institute of Technology, Cambridge, MA 02139, USA

^b Solar System Exploration Division, NASA Goddard Space Flight Center, Greenbelt, MD 20771, USA

^c Dept of Earth, Environmental and Planetary Sciences, Brown University, Providence, RI 02912, USA

^d Hawaii Institute of Geophysics and Planetology, University of Hawaii, Honolulu, HI 96822, USA

^e Department of Earth and Planetary Sciences, Weizmann Institute of Science, Rehovot 76100, Israel

^f School of Earth and Space Exploration, Arizona State University, Tempe, AZ 85287, USA

^g Stinger Ghaffarian Technologies Inc., Greenbelt, MD 20770, USA

^h Sigma Space Corporation, Lanham, MD 20706, USA

ⁱ German Aerospace Center (DLR), Rutherfordstrasse 2, 12489 Berlin, Germany

^j Technical University Berlin, D-10623 Berlin, Germany

^k School of Physics, Astronomy and Computational Sciences, George Mason University, Fairfax, VA 22030, USA

^l Space Department, The Johns Hopkins University Applied Physics Laboratory, Laurel, MD 20723, USA

^m Center for Research and Exploration in Space Science and Technology, University of Maryland, Baltimore County, Baltimore, 21250 MD, USA

ⁿ Division of Geological and Planetary Sciences, California Institute of Technology, Pasadena, CA 91125, USA

^o Lunar and Planetary Laboratory, University of Arizona, Tucson, AZ 85721, USA

^p Center for Earth and Planetary Studies, National Air and Space Museum, Smithsonian Institution, Washington, DC 20560, USA

ARTICLE INFO

Article history:

Received 14 March 2016

Revised 10 June 2016

Accepted 13 June 2016

Available online 25 June 2016

Keywords:

Moon
surface
orbit determination

ABSTRACT

In June 2009 the Lunar Reconnaissance Orbiter (LRO) spacecraft was launched to the Moon. The payload consists of 7 science instruments selected to characterize sites for future robotic and human missions. Among them, the Lunar Orbiter Laser Altimeter (LOLA) was designed to obtain altimetry, surface roughness, and reflectance measurements. The primary phase of lunar exploration lasted one year, following a 3-month commissioning phase. On completion of its exploration objectives, the LRO mission transitioned to a science mission. After 7 years in lunar orbit, the LOLA instrument continues to map the lunar surface. The LOLA dataset is one of the foundational datasets acquired by the various LRO instruments. LOLA provided a high-accuracy global geodetic reference frame to which past, present and future lunar observations can be referenced. It also obtained high-resolution and accurate global topography that were used to determine regions in permanent shadow at the lunar poles. LOLA further contributed to the study of polar volatiles through its unique measurement of surface brightness at zero phase, which revealed anomalies in several polar craters that may indicate the presence of water ice. In this paper, we describe the many LOLA accomplishments to date and its contribution to lunar and planetary science.

© 2016 Elsevier Inc. All rights reserved.

1. Introduction

The Lunar Reconnaissance Orbiter (LRO; Chin et al., 2007) was launched to the Moon on June 18, 2009 at 5:32 p.m. EDT (Vondrak et al., 2010). The purpose of the LRO mission was to obtain data about the Moon that will enable the future safe return of humans to the lunar surface, and to identify and characterize

* Corresponding author.

E-mail address: smithde@mit.edu (D.E. Smith).

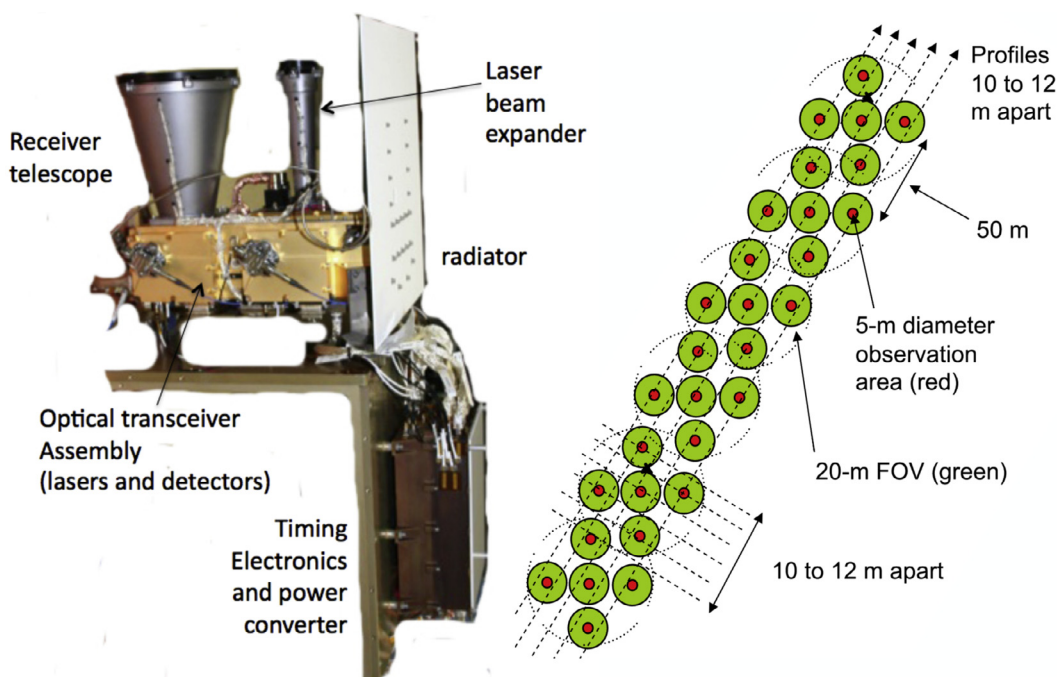


Fig. 1. The LOLA instrument (left) and the pattern of spots on the lunar surface (right). The red center spots are the areas illuminated by the laser and the green circles represent the fields of view of the corresponding detectors. (For interpretation of the references to color in this figure legend, the reader is referred to the web version of this article).

scientifically interesting landing site locations. These goals formed the basis of the selection of the instrument suite and the initial spacecraft orbit. The Lunar Orbiter Laser Altimeter (LOLA; Smith et al., 2010) is one of the seven instruments onboard LRO, and was designed to acquire substantial topographic measurements in order to provide accurate relief information and a geodetic reference frame for all high-resolution datasets acquired by the spacecraft.

LOLA uses short pulses from a solid-state laser through a Diffractive Optical Element (DOE) to produce a five-beam pattern that illuminates the lunar surface (Smith et al., 2010). LOLA makes four types of measurements: the range between the spacecraft and the surface, the energy of the laser pulse reflected from the surface, the width of the return laser pulse, and the solar radiation reflected from the lunar surface. From these basic measurements, several scientific datasets are derived, including the topography, the albedo at the wavelength of the laser (1064.4 ± 0.1 nm; Smith et al., 2010), the roughness of the lunar surface within the footprint of each laser spot, and the 1064-nm reflectance of sunlight from the lunar surface.

In addition, LOLA enabled a Laser Ranging (LR) investigation (Zuber et al., 2010) by which laser pulses from Earth-based satellite laser ranging stations to LRO provided one-way range measurement. A small optical receiver mounted on the Earth-pointed high-gain antenna received the 532-nm pulses, which were passed to LOLA for precise timing via a fiber optic cable. This experiment provided additional tracking for LRO and enabled, for the first time, routine laser tracking of a spacecraft in lunar orbit.

LRO was placed in its commissioning, near-polar, eccentric orbit with low periapsis (~ 30 -km altitude near the south pole) on June 27, 2009. Three months later, on September 27, the spacecraft entered its 50-km, near-circular mapping orbit, where it completed a one-year exploration mission for landing site characterization, and then started its science-driven mission. On December 11, 2011, the spacecraft was placed back in a near-frozen orbit (near constant periapse altitude and location) and altitude range of 30 km

Table 1

Instrument parameters and performance since start of operations, July 3, 2009, until March 1, 2016.

LOLA operation, 2009–2016	
Number of altimeter observations	6807,309,472
Number of laser firings	4000,021,600
Initial laser output (mJ)	2.5
Laser pulse rate (Hz)	28
Laser pulse width (ns)	5

to 200 km to save fuel and extend the lifetime of the mission. In the spring of 2015, the orbit periapsis was lowered to 20–40 km.

2. The LOLA instrument

The LOLA instrument, shown in Fig. 1, is a laser ranging device that splits a pulsed laser beam into five output beams via a Diffractive Optical Element (DOE), has a single receiver telescope, and a detector for each of the beams. The LOLA ground pattern provides 5 profiles spaced approximately 12 m apart cross-track with measurements separated by 57 m along-track for each profile (from the average 50 km altitude). Fig. 1 shows the ground pattern of observations. Each beam provides a measurement of the round-trip time of flight (range), pulse spreading (surface roughness), and transmit/return energy (surface reflectance at the laser wavelength). The laser pulse energy, the receiver aperture size, and the spacecraft altitude limit the range precision to about 10 cm for a flat surface. As a consequence of its two-dimensional spot pattern, the instrument provides an unambiguous determination of both along-track and cross-track slopes along the spacecraft ground track (Fig. 2). LOLA has operated nearly continuously (exceptions discussed later) since July 3, 2009 (Table 1).

Laser altimetry from orbit requires the position and attitude of the spacecraft, and the altimeter's laser beam pointing with respect to the spacecraft coordinate system. To that end, several experiments were conducted to measure post-launch instrument

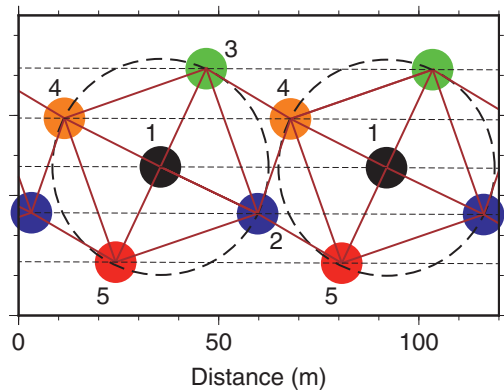


Fig. 2. Derivation of slopes from two consecutive laser pulse shots from LOLA's five-beam patterns showing an area $60\text{ m} \times 100\text{ m}^2$. Successive laser pulse firings from a 50-km orbital altitude (dashed circles) each illuminate five spots, for which the $\sim 57\text{ m}$ along-track separation provides independent one-dimensional profiles (dashed lines). Various baselines (red) can be used to estimate bi-directional slopes over 25-m baselines. Residuals from planes fit to four or more closely-spaced spots provide root-mean-square roughness estimates. (For interpretation of the references to colour in this figure legend, the reader is referred to the web version of this article).

characteristics of LOLA including the laser boresight vector. In these experiments, LRO pointed away from the Moon and scanned the Earth in a raster pattern, as the LOLA laser actively fired. A ground station on Earth received the 1064 nm pulses (the downlink), while it fired its own laser to LRO (the uplink). The downlink pulse arrival times and digitized waveforms were recorded at the ground station, the Goddard Geophysical and Astronomical Observatory (GGAO) in Greenbelt, MD, and the uplink arrival times and pulse widths were recorded by LOLA's five detectors.

Three successful LOLA active Earth scans were conducted: one in 2009, shortly after launch; one on Jan. 7, 2014; and another on Mar. 24, 2014. The 1.2-m telescope at GGAO was equipped to record the 1064-nm downlink pulse arrival times and to digitize the pulse waveforms. During post-processing, the energy of each downlink pulse could thus be measured by integrating the area under a Gaussian fit to the waveform. The spacecraft position and attitude were obtained from LRO project-supplied SPICE kernels. The fire times and receive times of the pulses were matched after

applying appropriate light time corrections. The time tags of the transmitted and the received laser pulses at both LRO and GGAO were used to solve for the LOLA bore-sight offset between the laser and the receiver field of view. Note, this is not related to the Blanket Anomaly discussed in Appendix where further details of the instrument performance are provided.

The use of altimetric crossovers provides another means to calibrate the post-launch laser beam boresight vector. Compared to single beam altimeters, the novel cross-track information provided by LOLA's multi-spot footprint allows a more accurate adjustment of crossover offsets, because each track's profile forms a narrow surface onto which the other track's points can be interpolated. A sample of nearly 800,000 daytime and nighttime crossovers acquired in the 50-km circular orbit was used to derive corrections to the nominal laser boresight vector. Mazarico et al. (2014) used those to study the lunar body tide (Section 3.8). For each crossover, the 3-dimensional offset vector between the tracks was adjusted until it minimized the elevation residuals. The adjustment reduced the median RMS elevation residual for all crossovers from 1.67 m to 0.48 m. Pointing errors cause periodic variations in the time series of cross-track and along-track offsets (Fig. 3). This periodic behavior is correlated with the day/night cycle and the semiannual LRO yaw flips (see Appendix). Modeling of this crossover offset time series yields daytime and nighttime corrections to the nominal boresight in the range of 45 to 275 μrad , which were incorporated into the LOLA data processing pipeline in July 2014 and into the subsequent LOLA PDS releases. The corrected nighttime boresight vector derived from this crossover analysis is in agreement with that derived from the Earth scans above. Future Earth scans when LOLA is illuminated will be useful to ascertain the post-launch daytime boresight.

LOLA's normal mode of operation is nadir-pointed, although it is also operated off-nadir when LOLA or another instrument is targeted to a location not directly under the spacecraft groundtrack. Off-nadir pointing is rather common, and part of the normal operations of the LRO spacecraft. LOLA can acquire data over all regions of the Moon, but because the groundtracks are closer at high latitudes than near the equator the spacing between LOLA measurements is much smaller at the poles than near the equator. Fig. 4 shows the average longitudinal coverage (distance between measurements) by latitude. The average coverage in latitude is generally on the order of 20 to 30 m (along-track), as a result of the pulse rate of 28 Hz and the 5 profiles.

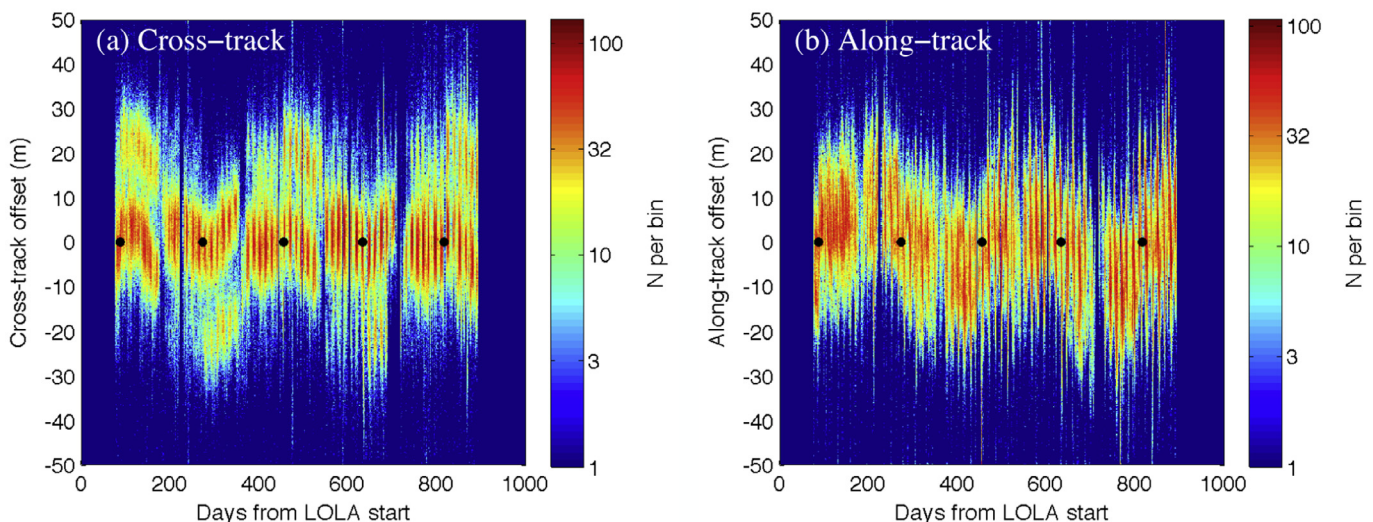


Fig. 3. Time series of (a) cross-track and (b) along-track LOLA beam offsets determined from crossovers. Black dots mark the semi-annual yaw flips of the LRO spacecraft.

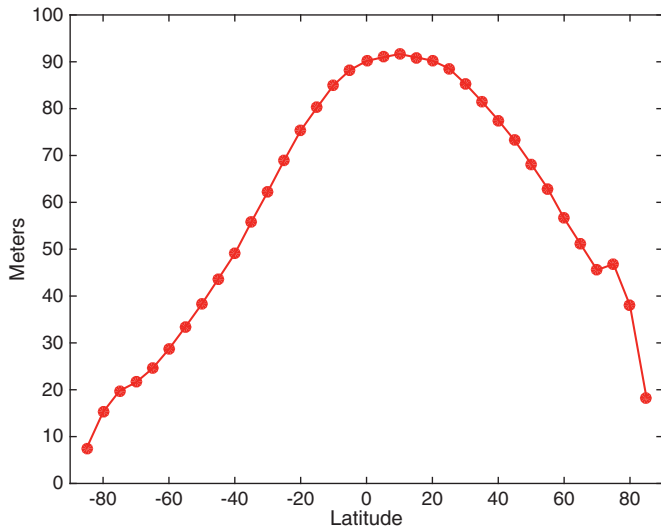


Fig. 4. LOLA's longitudinal spacing as a function of latitude. The mean longitudinal spacing is calculated from all valid ground returns within 50 m of each latitude shown.

Locally, the spacing varies and can be several times larger (or smaller) than the average of a given latitude. In addition, the average separation over the southern hemisphere is less, due to the increased operation time during the eccentric orbits both during commissioning in 2009 and since the fall of 2012 to conserve fuel. In the northern hemisphere, the present LRO altitude above the equator is generally greater than the range capability of LOLA, so few altimetric measurements can be obtained north of the equator.

3. Summary of science results

3.1. Global shape and topography

LOLA altimetry data have been assembled into global grids in cylindrical and polar stereographic projections, at a variety of resolutions (Smith et al., 2015). Densely-spaced altimetric data are binned into uniformly-sampled maps by median filtering to exclude noise returns. Recognizing that both manual inspection and automatic rejection of noise can be imperfect when the return rate is low (when LRO altitude is high), an additional comparison with stereophotogrammetric tiles (Barker et al., 2016a) is sometimes used in the eccentric orbit to exclude the remaining outliers. Data gaps in the maps are filled by interpolation using splines under tension (Smith and Wessel, 1990). The resulting maps are provided in multiple tiles at a resolution of 512 pixels per degree (ppd; equivalent to ~59 m resolution at the equator), as well as coarser versions re-sampled by powers of two. (A global grid at 1024 pixels per degree was deemed too sparse overall and has not been updated, although there are sufficient points to build denser grids in many regions.) While the near-polar LRO orbit yields the highest areal density of ground returns near the poles, the density of sampling is roughly uniform in a simple cylindrical projection. Interpolation using this projection does not perform well in preserving shapes of landforms near the poles, thus high-latitude ground points are binned, median-averaged and interpolated in conformal polar projections as well. Polar stereographic maps, which preserve circular landforms, are produced at resolutions from 5 to 80 m per pixel poleward of 80° latitude, from 30 to 120 m per pixel above 75°, from 60 m to 240 m per pixel above 60°, and from 100 to 400 m per pixel poleward of 45°. The LOLA Digital Elevation Models (LDEMs), are indexed by shaded-relief browse images, accom-

Table 2

Lunar spherical harmonic shape parameters. Values are given to four significant figures or tenths of meters, whereas the expansion is carried out at higher precision. Systematic errors on the order of 0.5 m are the dominant source of uncertainty. Shape parameters from the PDS product LRO_2050_SHA.TAB (Smith et al., 2015).

Parameter	Unnormalized (km)	^a Normalized (km)
Mean radius C_{00}	1737.1513 ± 0.0005	Same
C_{20} (flattening)	-1.4937	-0.6680
Polar radius (from C_{20})	1735.6576	
Equatorial radius	1737.8981	
Center of figure (X), C_{11}	-1.7756 ± 0.0005	-1.0251
Center of figure (Y), S_{11}	-0.7311 ± 0.0005	-0.4221
Center of figure (Z), C_{10}	0.2396 ± 0.0005	0.1383
C_{21}	-0.9933	-0.7694
S_{21}	0.02245	0.01739
C_{22}	0.0704	0.1091
S_{22}	0.2473	0.3832

^a Spherical harmonics are normalized at degree l and order m as $C_{lm} = N_{lm} C_{lm}$, where $N_{lm} = \{[(2-\delta_{m,0})(2l+1)(l-m)!]/(l+m)!\}^{1/2}$.

panied by count maps (LDEC) that show the number of returns in each pixel (a value of 0 where interpolation is necessary).

With the steadily improved knowledge of lunar gravity afforded by the Gravity Recovery And Interior Laboratory (GRAIL) Discovery Mission (Zuber et al., 2013a), systematic errors in orbital tracks have been largely eliminated (Mazarico et al., 2013), with the topographic uncertainty dominated by gaps in cross-track sampling. Such gaps are more frequent near the lunar limbs (90°E and 270°E), because spacecraft maneuvers were preferentially performed 'face-on' and precluded science measurements. Spacecraft attitude uncertainty also accounts for some geometric errors, especially during slews. At the 5-m resolution of the polar DEMs, small adjustments are still necessary to completely match adjacent tracks (Zuber et al., 2012; Gläser et al., 2014 and this issue).

Low altitude orbital surveys such as performed during the GRAIL mission end game demanded the best possible knowledge of topographic extremes to avoid prematurely impacting unsampled high-standing terrain. Prior to 2009, the global shape of the Moon (Smith et al., 1997) was uncertain by many hundreds of meters (Margot et al., 1999b), particularly over the farside highlands. The early results from the SELENE mission [Araki et al., 2009] gave a 19.8 km range of topography, while LOLA topographic extremes are about 19.92 km. The longest physical diameter, 3486.014 km, lies between 25.9°N, 204.15°E and its diametrically opposite point, while the shortest diameter, 3463.267 km, lies at 67.1°S, 179.7°E, subtending an angle of 94.8°. Relative to the IAU 1737.4-km-radius spherical datum, the deepest point, -9.129 km, lies at 70.36°S, 187.52°E, and the highest, 10.792 km, lies at 5.341°N, 201.37°E. The equatorial radius averaged over a 1° wide latitudinal band is 1738.133 km.

For comparison with the dynamical axes of a nearly-spherical body, it is conventional to use a spherical harmonic expansion to characterize the principal parameters of shape, as listed in Table 2. The degree 1 un-normalized coefficients represent the offset of the center of figure (COF) from the center of mass, and yield 1.935 km, chiefly in the -X (anti-Earth) direction (the longitude of the offset projected to the equatorial plane is 202.38°E). Although a reference ellipsoid of revolution (spheroid) has not been adopted, the degree (2,0) coefficient implies a flattening of 0.001289, considerably greater than that of a hydrostatic body under the influence of rotational and tidal potentials. Considering the degree and order (2,2) sectoral terms, the principal semi-axis of the shape is 1738.670 km at 143° longitude, and the intermediate semi-axis is 1737.127 km at 143° longitude, and the intermediate semi-axis is 1737.127 km, also offset from the principal dynamical axes. A tri-axial ellipsoid about the center of figure has dimensions of 1739.146, 1737.394, and 1734.928 km, although such a form represents shape poorly,

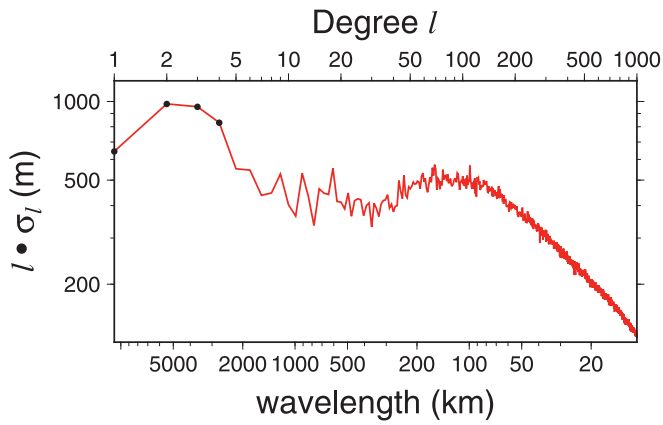


Fig. 5. Spherical harmonic topographic coefficient root mean variance by degree (logarithmic scale). The root sums $\sigma_l = [\sum C_{lm}^2 / (2l+1)]^{1/2}$ of normalized coefficients are multiplied by degree for illustration.

with a root-mean-square misfit of 1.73 km; its major axis is tilted 27° with respect to the pole of rotation. As we illustrate below, the shape is strongly perturbed by long-wavelength effects.

The topographic power spectrum of the Moon is shown in Fig. 5. Spherical harmonic coefficients of degree 1–4 (dots) dominate the shape. At wavelengths of ~ 90 to 2000 km (degrees 5–120), topographic power is diminished relative to the power law behavior at higher degrees, corresponding to a transition from complex craters to basin morphology and flexural isostatic compensation.

Fig. 6a shows the global topography of the Moon centered on 270°E with Orientale basin prominent below the equator. Each succeeding Fig. 6(b–d) removes successive low-degree terms up to 4. The nearside Mare Procellarum region and the farside South Pole-Aitken impact basin account for much of the low-degree signal (Garrick-Bethell et al., 2014; Keane and Matsuyama, 2014). The residual figure is shaped by more than 70 basin-scale impact structures (Neumann et al., 2015) as well as finer scale-positive-relief features – the topographic rims of craters or to a lesser extent the volcanic features such as the Aristarchus and Marius hills, and Montes Rumker, Mairan, Gruithuisen and Carpatas. Wrinkle ridges and other tectonic features in the nearside mare regions also exhibit positive relief.

3.1.1. Regional topography

Regional geological studies are enabled by LOLA topography in regions where partial or permanent shadow preclude other observations, such as over the floor of the 136-km-diameter Antoniadi Crater on the southern farside, in a region of very thin crust. The topography of this transitional-type basin, with terraced walls, an interior peak ring and a small central peak, is shown in Fig. 7a. The area shown covers about 0.06% of the Moon. The lowest elevation of the Moon lies at the bottom of a ~ 15 -km diameter simple crater within Antoniadi at 70.36°S , much of which exists in permanent shadow. Altimetry, however, reveals several features of its floor. These observations constrain the scale at which morphological transitions occur in this unusually deep region of the Moon.

Within the visible portions of Antoniadi, the location of an image (M154024477R) taken by the LROC NAC camera (Robinson et al., 2009) of a km-sized mound outcropping from the crater floor is outlined by a small square (Fig. 7c). Fig. 7b and d illustrates how the LOLA data provide context for interpretation of such features. Here the ~ 20 m resolution afforded by many closely-spaced groundtracks allows profiles and contours to assess the height of very small, unusual features, and resolve a few-meters-deep moat surrounding the 60-m-high mound.

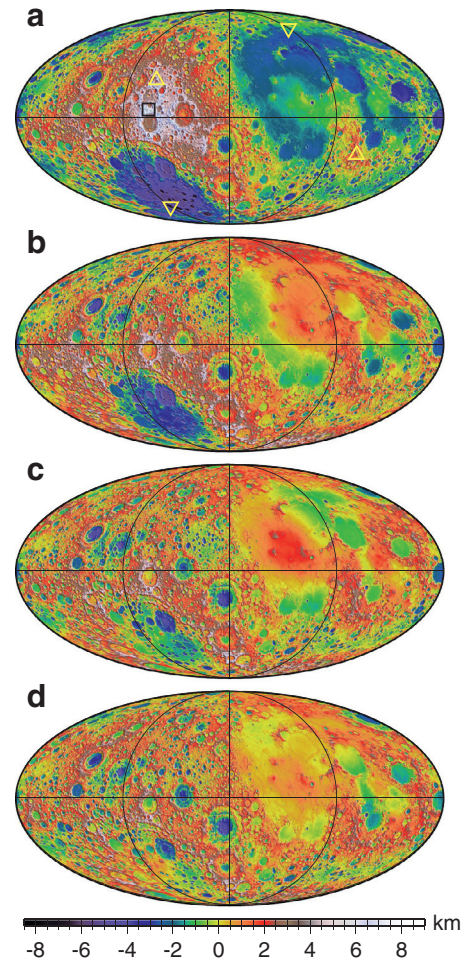


Fig. 6. (a) Global topography of the Moon in Mollweide equal-area projection, centered at 270°E longitude, with the color scale at bottom superposed on hill-shaded relief. A black square denotes the highest point on the northern rim of Korolev, while yellow triangles denote the axes of the greatest and smallest diameters through the center of mass. Subsequent figures show high-pass topography from (b) degree 3 (c) degree 4, and (d) degree 5 upwards. (For interpretation of the references to color in this figure legend, the reader is referred to the web version of this article).

3.2. Global roughness and surface slopes

Quantification and analysis of surface roughness properties of the Moon at unprecedented scales and resolution are made possible with the new global elevation data. Surface slope and roughness can be measured at the 100-m scale with about 10 altimetric points (2 LOLA frames), by fitting a plane and measuring their scatter around it (Fig. 8). Rosenberg et al. (2011) further mapped lunar surface slope and roughness using a range of parameters: median absolute slope, both directional (along-track) and bidirectional (in two dimensions); median differential slope; and Hurst exponent, over baselines ranging from ~ 17 m to ~ 2.7 km. Rosenberg et al. (2011, 2015) found that the lunar highlands and the mare plains display vastly different roughness properties, with less distinctive variations within mare and highlands. Most of the lunar surface exhibits fractal-like behavior (cf. Turcotte, 1987), with a single or two different Hurst exponents over the given baseline range; when a transition exists, it typically occurs near the 1-km baseline, indicating a significant characteristic spatial scale for competing surface processes. Rosenberg et al. (2011) found that the Hurst exponent is high within the lunar highlands, with a median value of 0.95, and lower in the maria (with a median value of 0.76).

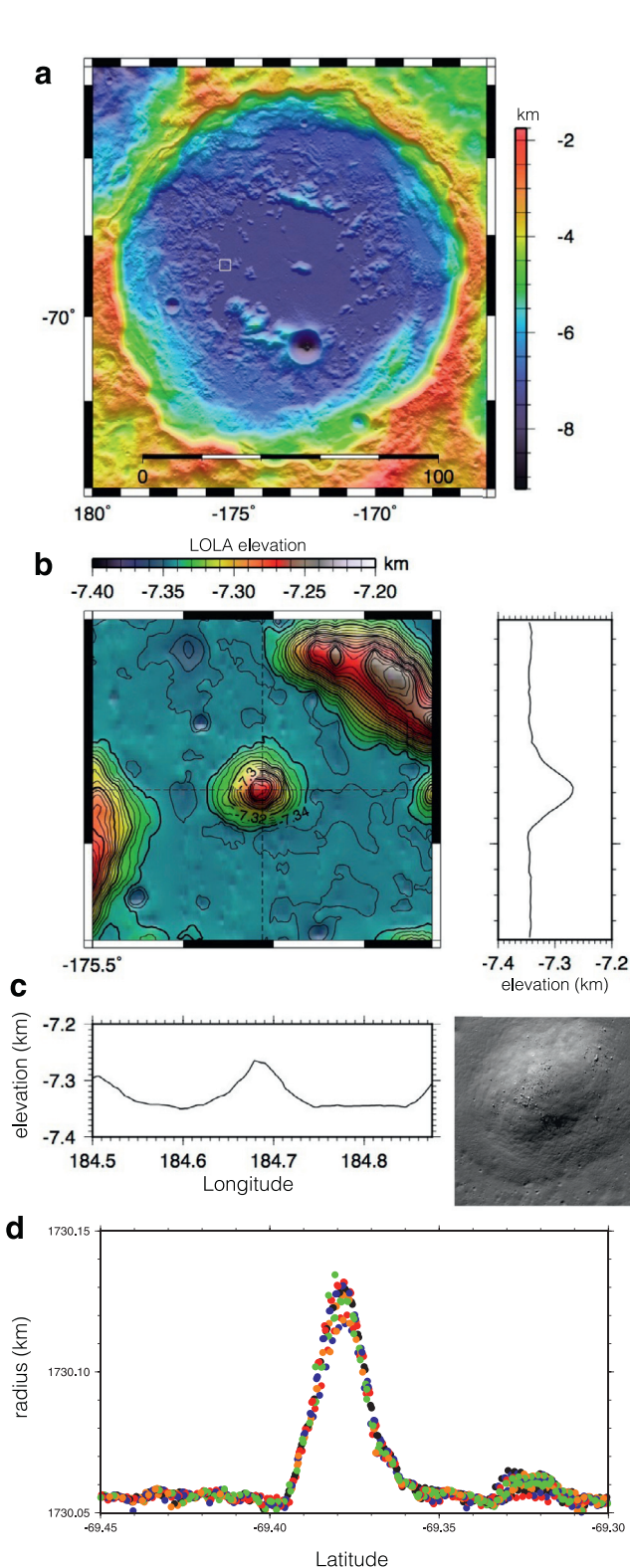


Fig. 7. (a) Shaded-relief topography of Antoniadi Crater, a 141-km-diameter impact feature that is the deepest feature of its size on the Moon. The white square outlines a small mound on the floor. (b) Contour plot at 5-m intervals showing the height of the mound from the LOLA LDEM_512_90S_45S_180_270 product, and profiles sampled from the gridded data record along N-S and E-W lines (vertical exaggeration 6:1). (c) The 3-km-diameter mound as seen by the LROC NAC (image M154024477R). (d) North-South profile across the mound showing individual LOLA returns (color indicates detector number) (vertical exaggeration 25:1). (For interpretation of the references to color in this figure, the reader is referred to the web version of this article).

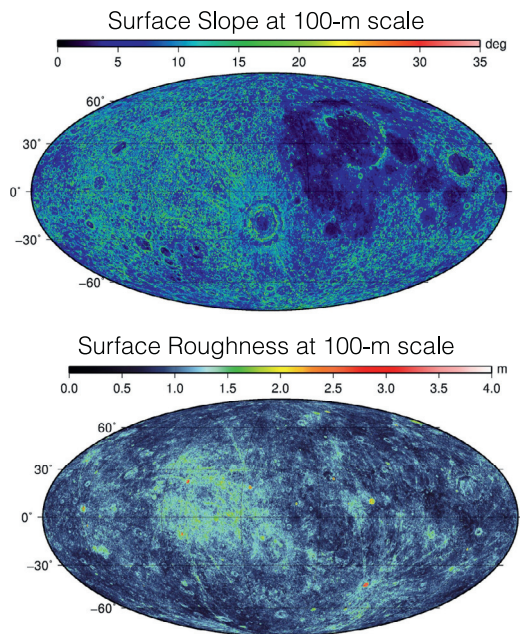


Fig. 8. Surface slope (top) and roughness (bottom) at hectometer scale derived from pairs of LOLA shots (~10 points).

Rosenburg et al. (2011) demonstrated that the median differential slope is a powerful tool for discriminating between roughness units and is useful in characterizing the ejecta surrounding large basins, particularly Orientale, as well as the ray systems surrounding young, Copernican-age craters. They further show that median differential slope allows a quantitative exploration of the evolution of surface roughness with age on mare surfaces.

In further analysis of the altimetry data, Kreslavsky et al. (2013) presented maps of the topographic roughness of the Moon at hectometer and kilometer scales derived from range profiles obtained by LOLA. As roughness measures, they used the interquartile range of profile curvature at several baselines, from 115 m to 1.8 km, and plotted these in a global map format. The maps provide a synoptic overview of variations of typical topographic textures and utilize the exceptional ranging precision of the LOLA instrument. Kreslavsky et al. (2013) found that hectometer-scale roughness poorly correlates with kilometer-scale roughness, because the two scale lengths reflect different sets of processes and time scales. Hectometer-scale roughness is controlled by regolith accumulation and modification processes and affected by the most recent events (primarily, geologically recent (1–2 Ga) meteoritic impacts). Kilometer-scale roughness, on the other hand, reflects major geological (impact, volcanic and tectonic) events in earlier geological history. The data presented by Kreslavsky et al. (2013) also show that young large impact craters are rough, and their roughness decreases with increasing age. The global roughness maps reveal a few unusually dense clusters of hectometer- and decameter-size impact craters that differ in their morphology and settings from typical secondary crater clusters and chains; the origin of these features is currently unknown. Kreslavsky et al. (2013) maps can also assist in the geological mapping of the lunar maria by revealing contacts between volcanic plain units. The global roughness maps also clearly reveal cryptomaria, old volcanic plains superposed by younger materials, primarily crater and basin ejecta (Whitten and Head, 2013, 2015a,b).

Furthermore, these data can be successfully applied to understanding the dynamics of impact processes and their effects on surface degradation, even at planetary scales. Kreslavsky and Head (2012) showed that the new maps of kilometer-scale topographic

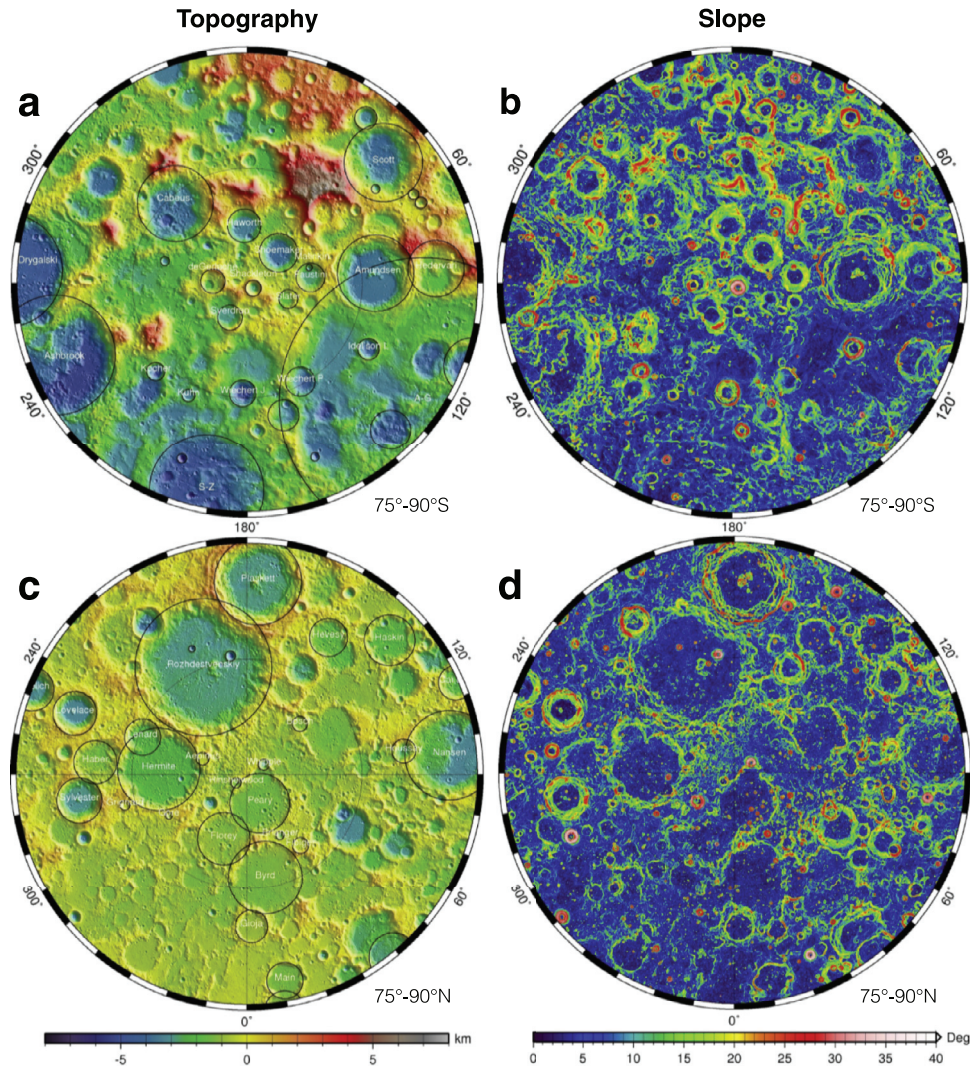


Fig. 9. Topography (a, c) and 100-m baseline surface slopes (b, d) of the lunar south and north poles, respectively. The topography clearly shows the variations in elevation while the slopes better define the edges of craters and ridges, and the flatness of crater floors. Both maps extend from 75° to the pole.

roughness and concavity of the Moon reveal a distinctive roughness signature of the proximal ejecta deposits of the Orientale basin (the Hevelius Formation). They found that no other lunar impact basin, even the just-preceding Imbrium basin, is characterized by this type of signature although most have similar types of ejecta units and secondary crater structures. The preservation of this distinctive signature, and its lack in basins formed prior to Orientale, was interpreted by [Kreslavsky and Head \(2012\)](#) to be the result of seismically-induced smoothing caused by this latest major basin-forming event. Intense seismic waves accompanying the Orientale basin-forming event preceded the emplacement of its ejecta in time and operated to shake and smooth steep and rough topography associated with earlier basin deposits such as Imbrium. In their interpretation, Orientale ejecta was emplaced immediately following the passage of the seismic waves and thus formed the distinctive roughness signature that has been preserved for almost 4 billion years.

3.3. Polar topography and slopes

Because of the dense spatial coverage afforded by LRO's polar orbit, the north and south polar regions are characterized by a high density of ground track coverage that has enabled high resolution

maps. [Fig. 9](#) shows topography and 100-m slopes for the north and south polar regions. These topographic maps shown have a spatial resolution of 60 m that enables geologic characterization relevant for science analyses and exploration planning. The highest-resolution polar maps (5 m/pixel from 87.5° latitude to each pole) met the mission requirement of 30-m resolution for locations of potential landing sites or regions of special scientific interest.

LOLA high-resolution DEMs enable geologic characterization as well as crater counting and relative age dating of the lunar poles, including permanently shadowed areas. A prominent example is Shackleton crater, which is nearly coincident with the Moon's south pole. Its interior receives almost no direct sunlight and is a perennial cold trap, making it a promising candidate location in which to seek sequestered volatiles. Previous orbital and Earth-based radar mapping and orbital optical imaging, however, have produced conflicting interpretations about the existence of volatiles ([Nozette et al., 2001](#); [Campbell et al., 2006](#); [Haruyama et al., 2008](#); [Spudis et al., 2013](#)). The observations of [Zuber et al. \(2012\)](#) from LOLA DEMs, ([Fig. 10](#)) revealed Shackleton to be an ancient, unusually well-preserved simple crater whose interior walls are fresher than its floor and rim. The LOLA DEMs show that Shackleton floor deposits are nearly the same age as the rim, suggesting that little floor deposition has occurred since the crater

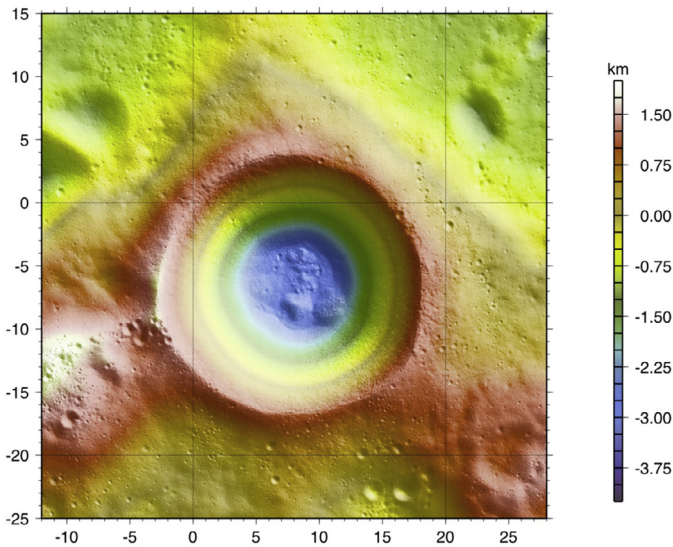


Fig. 10. Topographic map and topographic image of Shackleton Crater using LOLA data. Topography and slopes are based on a 10-m spatial resolution grid of all available LOLA profiles that include collectively 16 million unique elevation measurements. Elevations are contoured at 5-m intervals (Zuber et al., 2012).

formed more than three billion years ago. At the LOLA laser wavelength, the floor of Shackleton is brighter than the surrounding terrain and the interiors of nearby craters, but not as bright as the interior walls. Zuber et al. (2012) interpreted these combined observations to be explained primarily by downslope movement of regolith on the walls, exposing fresher underlying material (Fassett and Thompson, 2014). The relatively brighter crater floor is most simply explained by decreased space weathering due to shadowing, but a one-micrometer-thick layer containing about 20 percent surficial ice was cited as an alternative possibility.

LOLA high-resolution DEMs have also been analyzed to assign ages to other South circumpolar permanently-shadowed crater interiors. Tye et al. (2015) studied the interiors of the lunar south circumpolar craters Haworth, Shoemaker, Faustini, and Shackleton, all of which contain large permanently shadowed regions (PSRs) and all have been interpreted to contain sequestered volatiles including water ice. LOLA altimetry data provided a new means of examining the permanently shadowed interiors of these craters in unprecedented detail. Tye et al. (2015) used extremely high-resolution gridded LOLA data to determine the size-frequency distributions and the spatial density of craters superposing their rims, inner slopes, and floors. On the basis of their population of superposed craters, Haworth, Shoemaker, and Faustini have pre-Nectarian formation ages. Shackleton was interpreted as having a Late Imbrian age on the basis of craters superposed on its rim. Using LOLA slope data, Tye et al. (2015) showed that the local density of craters is strongly dependent on slope; because of its steep interior slopes, the lifetime of craters on the interior walls of Shackleton is limited. The slope-dependence of the small crater population implies that the population in the size range analyzed is controlled primarily by the rate at which craters are destroyed, consistent with the hypothesis that crater removal and resurfacing is a result of slope-dependent processes such as diffusive mass wasting and seismic shaking.

3.4. Radiometry, reflectance and albedo

3.4.1. Normal albedo from active radiometry

Owing to the importance of ice as a potential resource at the lunar poles, LOLA was designed to search for deposits of surface

frost in regions of permanent shadow through measurement of the reflectance of the surface at 1064 nm (Smith et al., 2010). Because LOLA provides its own light source, its measurements are particularly useful because reflectance measurements within regions of permanent shadow can be compared quantitatively to those of the rest of the Moon without the need for complex photometric models that correct for variable lighting, or in the case of the regions of permanent shadow, indirect lighting. This attribute of LOLA is particularly useful for regions in permanent shadow, whose only natural light source in the visible portion of the spectrum, scattered light, is challenging to model as it depends on the topography and albedo within and around the shadowed regions.

Another useful feature of the LOLA reflectance experiment is that it measures the lunar surface reflectance at zero phase angle, that is the angle between the light source (LOLA's laser transmitter), the lunar surface, and the receiver (LOLA's receiver telescope) is zero (or effectively so, there is a minute angle due to the travel time of the light pulse to the lunar surface and back). With the Sun as a light source, this zero phase angle condition can sometimes be observed from the Earth and from space, but because the angle of incidence systematically increases toward the poles, the surface is increasingly foreshortened and passive zero-phase measurements in polar craters are not possible. For a dark surface like the Moon, measurements at zero phase are free of dependence upon topography, again enabling comparison of reflectance measurements among terrains without the need for photometric models. Fig. 11 shows the lunar albedo at 1064 nm derived from the LOLA active reflectance measurements.

The initial results from the LOLA reflectance experiment found that the south polar crater Shackleton, mostly in permanent shadow, was locally unique in reflectance, being substantially brighter than its surroundings. Zuber et al. (2012) considered several hypotheses for this anomalous reflectance, including but not limited to the presence of surface frost. Calibration of the first year of LOLA observations demonstrated that regions in permanent shadow are in general about 15% brighter than polar areas that receive some illumination and Lucey et al. (2014) suggested this general increase was due to inhibited space weathering owing to low temperatures, or possible surface frost.

Reflectance data from LOLA were used by Hemingway et al. (2015) and Lemelin et al. (2016) to show that the lunar maria exhibit a latitude-dependent albedo. They suggested this was due to a variation in space weathering with latitude and average solar incidence angle, supporting a sputtering source for lunar space weathering optical effects. LOLA's data uniquely supported this investigation because of its immunity from latitude-dependent photometric effects.

LOLA's measurements of the zero-phase reflectance are mirrored on the planet Mercury with the Mercury Laser Altimeter data (Neumann et al., 2013). Comparison of these two experiments show that the typical reflectance of Mercury is similar to that of the iron-rich lunar maria, despite the low-iron nature of the surface of Mercury. While this albedo difference was previously known, the laser experiments provide robust independent confirmation, and a unique photometric geometry to support investigations aimed at understanding the difference.

Ongoing experiments with LOLA reflectance now center on a search for time-variable reflectance which would help identify the cause of increased brightness in shadowed regions since any periodic variation is most likely due to transient surface frost. Data from Deep Impact, Cassini and Chandrayaan-1 indicated that spectral absorption due to water is time-variable on the lunar surface (Sunshine et al., 2009; Clark, 2009; Pieters et al., 2009). LOLA measurements of the reflectance of surfaces at a variety of temperatures may be able to detect or place upper limits on the abundance of migratory water or time-variable surface frost.

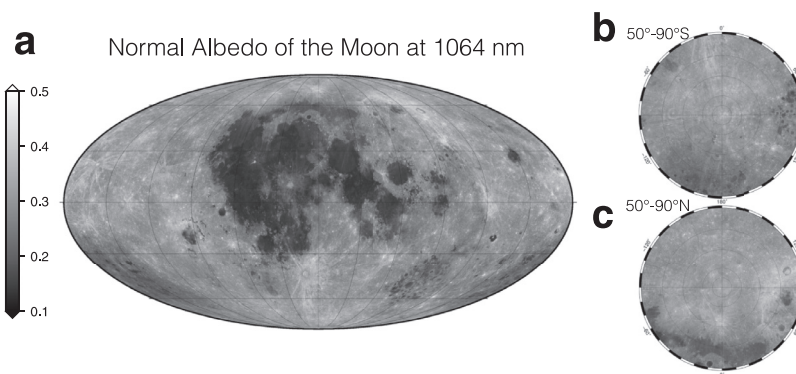


Fig. 11. Normal albedo of the Moon at 1064 nm from active radiometry. The surface resolution is approximately 5 km in the global map (a) and 1 km in the south (b) and north (c) polar maps. Adapted from [Lucey et al. \(2014\)](#).

3.4.2. Lunar phase function in the near-IR from passive and active radiometry

Although not included in the original instrument mission goals, we have developed a second reflectance measurement technique, which leverages the LOLA noise-monitoring house-keeping data and uses them as a unique passive radiometry science measurement of the Moon. Instead of letting the flight software control the thresholds to maintain the noise level to $\sim 1\text{--}2\%$ as during normal altimetric operations, the thresholds can be held fixed at very low levels to allow thousands of noise counts per second to be measured and yield high-SNR reflectance measurements. This threshold setting is typically only employed when the spacecraft is too high to otherwise obtain any altimetric measurement (northern hemisphere in the near-frozen elliptical orbit) and when the beta angle (angle between the prime meridian and the Sun) is not favorable considering the LOLA thermal blanket anomaly ($\beta \geq 80^\circ$) (see Appendix). This data set is unique because it covers a narrow spectral band, it is as precisely geolocated as the altimetry data, and it complements the active normal albedo measurement made with the laser. With passive radiometry, the instrument measures the solar photon rate reflected off the surface, which depends on the topography and viewing/illumination geometry. The so-called phase function describes the phase-angle portion of this dependence ([Fig. 12](#)). The phase function is of interest for better understanding the geologic and space weathering influences on regolith characteristics. A significant challenge has been to predict the observed variations in phase function with location and wavelength from first principles, because of the complexities of radiative transfer theory applied to lunar regolith. The unique ability of LOLA to measure the normal albedo through active reflectance provides new opportunities in this arena, because it allows for the removal of most of the effects of single particle albedo on the phase function from those of other regolith properties, such as the single particle backscattering strength and the opposition effect (OE, which is the surge in brightness at phase angles near zero).

[Barker et al. \(2016b\)](#) presented a method for calibrating the passive radiometry data and used the passive and active radiometry to study the near-IR phase function's dependence on various geologic parameters. On a global scale, they found that iron abundance and optical maturity were the dominant controlling parameters. Titanium abundance, surface roughness on decimeter to decimeter scales, and soil thermophysical properties had a smaller effect, and the latter two were correlated with optical maturity, indicating that exposure age was the driving force behind

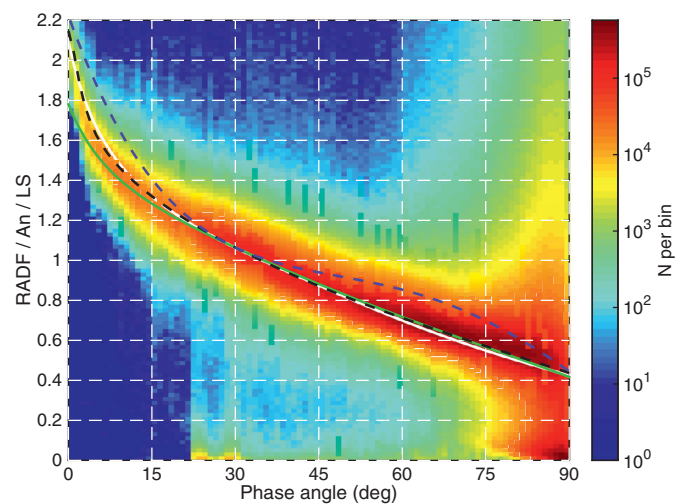


Fig. 12. 1064-nm highlands phase function from LOLA passive and active radiometry. Several phase functions for the highlands from the literature are overlaid and normalized at 30° phase: Clementine 950-nm (dashed black line; [Shkuratov et al., 1999](#)), LROC WAC 689-nm (solid white line; [Sato et al., 2014](#)), Spectral Profiler 1068 nm (solid green line; [Yokota et al., 2011](#)), and Chandrayaan-1 M3 1070 nm (dashed blue line; [Besse et al., 2013](#)). The vertical axis is the radiance factor (RADF) divided by the normal albedo (A_n) and the Lommel-Seeliger (LS) relation. The radiance factor is the reflectance relative to a perfectly diffuse surface illuminated vertically. Dividing RADF by A_n and LS corrects, respectively, for different intrinsic reflectances of the observation locations and for the effects of varying incidence and emission angles ([Hapke, 2012b](#)). (For interpretation of the references to color in this figure legend, the reader is referred to the web version of this article).

their contribution. The phase function also exhibited a dependence on slope, possibly due to mass wasting and/or reduced sky visibility. Geologically-influenced variations of the phase function were observed, in particular associated with the dark halo of impact melt around the Copernican-aged Jackson crater and the Reiner Gamma Formation (RG). The phase function of RG deviated from the global average (for the same composition and optical maturity), suggesting that the unusual regolith evolution and properties at this location affect the visible-to-near-IR spectrum and phase function differently. From detailed modeling of the photometric function, [Barker et al. \(2016b\)](#) verified that several wavelength trends observed by [Sato et al. \(2014\)](#) with LROC in the UV-VIS continue into the near-IR. In particular, the maria exhibited

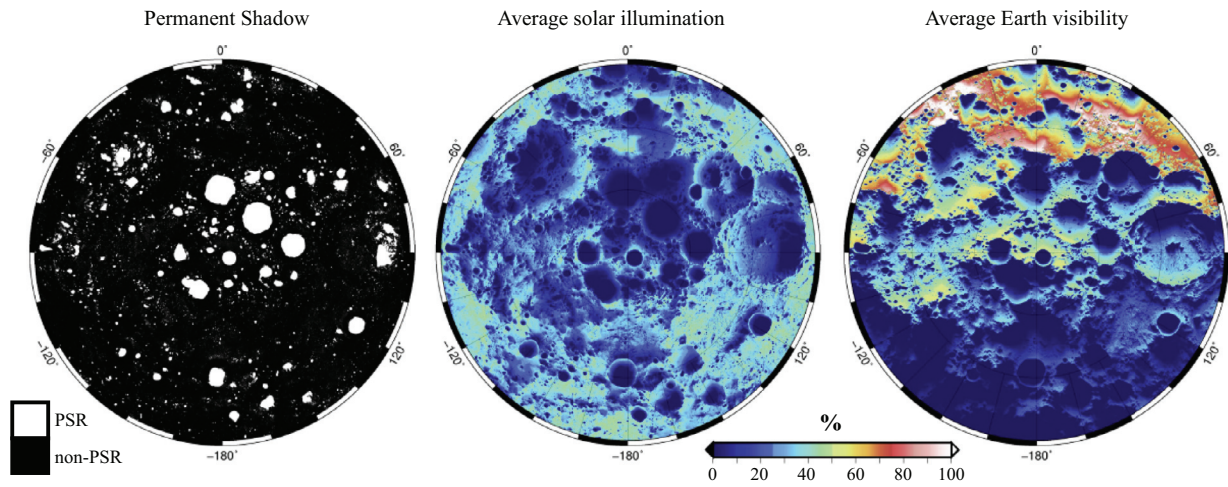


Fig. 13. Solar illumination modeling results based on a 60 m/px LOLA topographic map, over 82.5°S–90°S. (Mazarico et al., 2011a).

decreased backscattering, a narrower OE angular width, and a smaller OE amplitude relative to the highlands. It was also found that the backscattering strength and OE width have no significant correlation with geologic context within the maria.

These results shed further light on the wavelength dependence of the Moon's photometric behavior, something for which our theoretical understanding is presently incomplete (e.g., Hapke et al., 2012a). Altogether, compositional variations and space weathering have important effects on the Moon's photometric behavior apart from their influence on single particle albedo, a result made possible by LOLA's unique ability to directly measure normal albedo. Thus, laser altimeters like LOLA can contribute to photometric studies thanks to their combined active and passive radiometry measurements at all phase angles.

3.5. Illumination conditions at the lunar poles

One of the main objectives of the LRO mission was to study the distribution of volatiles and the processes controlling their presence and their potential time-variable transport.

Prior to the LRO mission, the existence of areas in 'permanent shadow' in the polar regions, hypothesized by Watson et al. (1961), was thought to be directly responsible, through cold-trapping, for all the volatiles observed by Lunar Prospector (Feldman et al., 1998). Spatially resolved observations by the LEND instrument on LRO (Mitrofanov et al., 2010) showed that the hypothesized correlation does not necessarily hold at small scales, and much work based on the new LRO datasets has focused on refining models of volatile production and loss (e.g., Farrell et al., 2015) and transport (Schorghofer and Aharonson, 2014).

Precise knowledge of the topography of the Moon is key in enabling these studies, as it directly impacts the illumination conditions and thermal environment of the lunar surface. The Clementine altimetric data (Smith et al., 1997) were not of sufficient quality to enable numerical simulations of the illumination conditions, and despite high intrinsic resolution, Earth-based radar data (e.g., Margot et al., 1999) were lacking uniform coverage due to the tidal lock of the Moon, resulting in significant coverage gaps and biases over a wide range of solar longitudes. While imagery-based studies did make progress in identifying areas of permanent shadow and of high illumination (Bussey et al., 1999), the laser altimeter data acquired by LALT (Araki et al., 2009) onboard SELENE enabled the first faithful simulation of illumination conditions based on a topographic model alone (Noda

et al., 2008). Soon after, the LOLA data substantially improved the quality and spatial extent made possible through numerical simulation, thanks to a longer mission duration and higher measurement rate (140 Hz effective). Mazarico et al. (2011a) presented results of solar insolation, permanent shadow regions (PSR) inventory, areas of highest illumination, and Earth visibility, over both poles (75–90°) at 240 m/px. Instead of the more traditional ray-tracing method, they used a 'horizon method', more efficient when investigating illumination conditions at finer temporal resolution over long temporal baselines. Individual timestep results were validated with concomitant LROC WAC images (Robinson et al., 2009). Fig. 13 illustrates such results, from a more recent simulation performed in the 82.5°S–90°S region at 60 m/px: average solar illumination and Earth visibility over a lunar nutation cycle (~18.6 years) and the areas determined to be in permanent shadow.

While spacecraft imagery ultimately provides ground truth for the illumination state (Speyerer and Robinson, 2013), camera observations are limited in temporal extent (by the mission duration) and in spatial extent (by spacecraft orbital phasing and instrument field of view), and thus do not necessarily suffice to investigate long-term or secular effects. The LOLA-derived illumination maps are useful for the interpretation and analysis of scientific data acquired by the other LRO instruments. For example, Mitrofanov et al. (2010) used the outlines of the PSRs defined by Mazarico et al. (2011a) to compute the statistical significance of the neutron suppression within them. The average illumination maps were leveraged in studies to better understand the distribution of volatiles in the near-subsurface, in particular by correlating the LEND measurements with illumination. Fig. 14 shows the high correlation between the general trends with latitude of decreasing average illumination poleward with the reduction in neutron counts as measured by both the Lunar Prospector Neutron Spectrometer (LPNS) and the Lunar Exploration Neutron Detector (LEND) (Mazarico et al., 2011a). Further studies further established this link, and showed the importance of maximum slope and slope azimuth on the presence of subsurface volatiles (McClanahan et al., 2015). Another derived product, the so-called sky visibility that describes the sky solid angle visible from the surface, was important to correct the Lyman Alpha Mapping Project (LAMP) observations and measure the surface albedo at UV wavelengths (Gladstone et al., 2012). Simulations over larger areas and at higher resolutions have since been performed. PSRs were identified at non-polar latitudes (Mazarico et al., 2011b), as low as 58.185°S

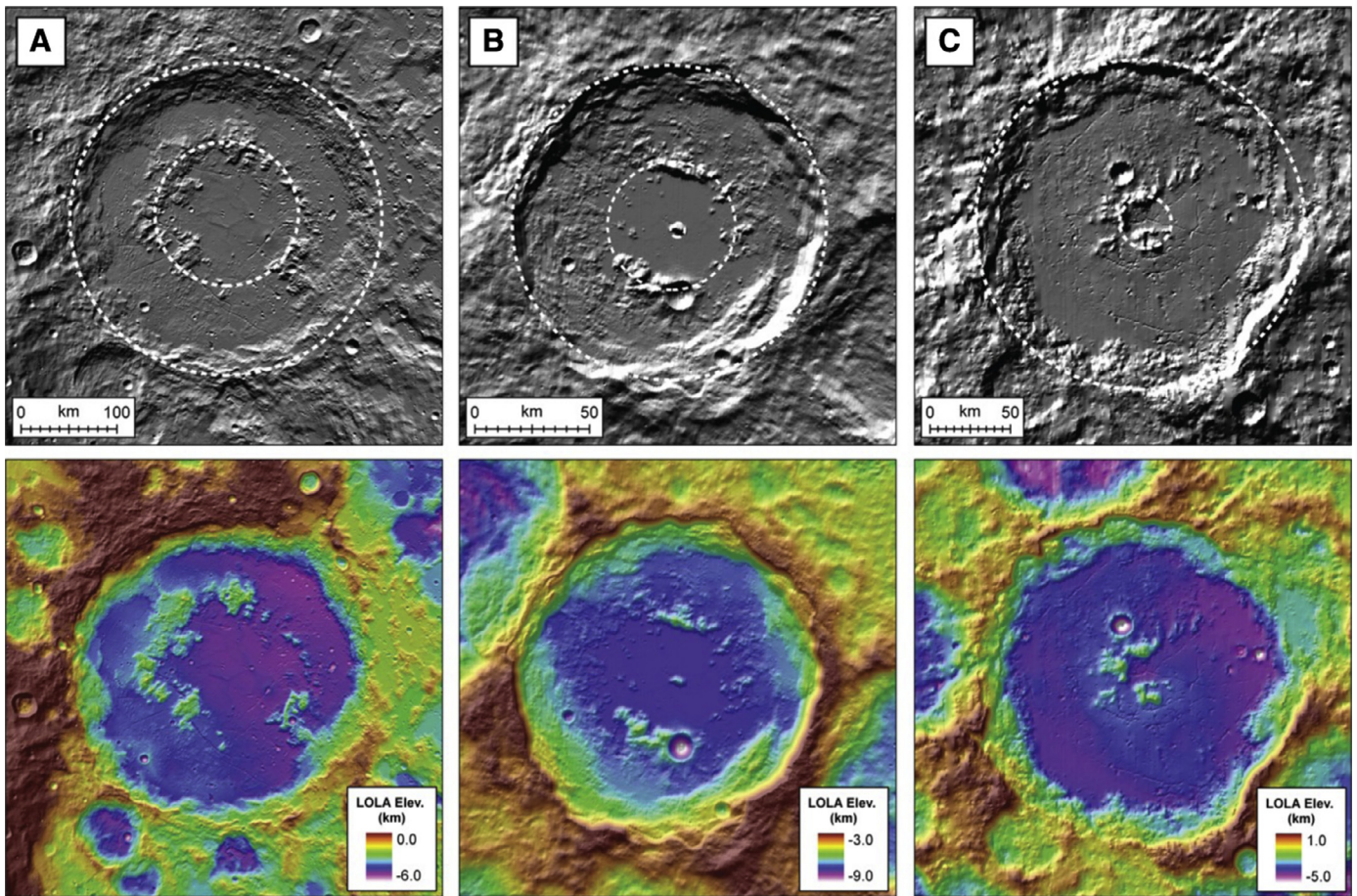


Fig. 14. Examples of a peak-ring basin (A), protobasin (B), and ringed peak-cluster basin (C) on the Moon. Top panels show outlines of circle fits to the basin rim crest and interior ring (dashed lines) on LOLA hillshade gridded topography. Bottom panels show LOLA colored gridded topography at 128 pixel/degree on LOLA hillshade gridded topography. (A) Schrödinger (326 km; 133.53_E, 74.90_S), a peak-ring basin, exhibits a nearly continuous interior ring of peaks with no central peak. (B) Antoniadi (137 km; 187.04_E, 69.35_S), a protobasin, has a less prominent peak ring surrounding a small central peak. (C) Humboldt (205 km; 81.06_E, 27.12_S) is a ringed peak-cluster basin with an incomplete, diminutive ring of central peak elements. From Baker et al. (2011). (For interpretation of the references to color in this figure legend, the reader is referred to the web version of this article).

and 58.412°N (McGovern et al., 2013). Gläser et al. (2014) used LROC NAC-derived shape models in combination with LOLA data to determine the best South Pole locations for landers, in terms of solar power input for future lunar exploration.

Continued work also showed that the total amount of area found to be in permanent shadow increases as the topographic map quality and the topographic resolution improve. Fig. 13 summarizes the extent of permanent shadow in the polar regions from various simulations. It illustrates that while Mazarico et al. (2011a) found that 7.03% and 9.82% of latitudes poleward of 85° (North and South, respectively) were in permanent shadow, a simulation at the same resolution (240 m/px) using the most recent LOLA map (PDS release 15, in June 2015) yields 7.75% and 10.19%. Higher resolutions (120 m/px and 60 m/px, with the same 2015 dataset) yield 8.79%/10.74% and 9.70%/11.41%, respectively. At even higher resolution, the trend continues, with ~25% more area in permanent shadow at 20 m/px than at 60 m/px. This is consistent with the fractal nature of topographic surfaces (Turcotte, 1987) and recent work by Bandfield et al. (2015) on thermal anisotropy. Conversely, as resolution increases, the most illuminated sites tend to shrink spatially and show lower solar illumination averages. No peak of eternal light, again hypothesized by Watson et al. (1961), exists on the Moon (Noda et al., 2008; Mazarico et al., 2011a; Gläser et al., 2014).

3.6. Geology

3.6.1. Morphometric characterization craters and basins

Of fundamental importance to the understanding of the geological evolution of planets is the quantitative nature of their landforms and their relationship to the thermal evolution of the planet. LOLA data have provided the basis to undertake these types of analyses, and to improve our knowledge of the origin and evolution of landforms related to impact crater volcanism and tectonism.

For example, a major question in the origin and evolution of impact craters and basins is the nature of the transition, with increasing size, from simple, to complex, to peak-ring basins and finally to multi-ring basins. Baker et al. (2011) used LOLA and LROC data to document the relationship between complex craters with central peaks and multi-ring basins in protobasins (exhibiting a rim crest and interior ring plus a central peak) and peak-ring basins (exhibiting a rim crest and an interior ring). New data have permitted improved portrayal and classification of these transitional features on the Moon. Using high-resolution LOLA gridded topographic data combined with image mosaics, Baker et al. (2011) conducted a survey of craters > 50 km in diameter on the Moon and updated the existing catalogs of lunar peak-ring basins and protobasins (see also Kalynn et al., 2013).

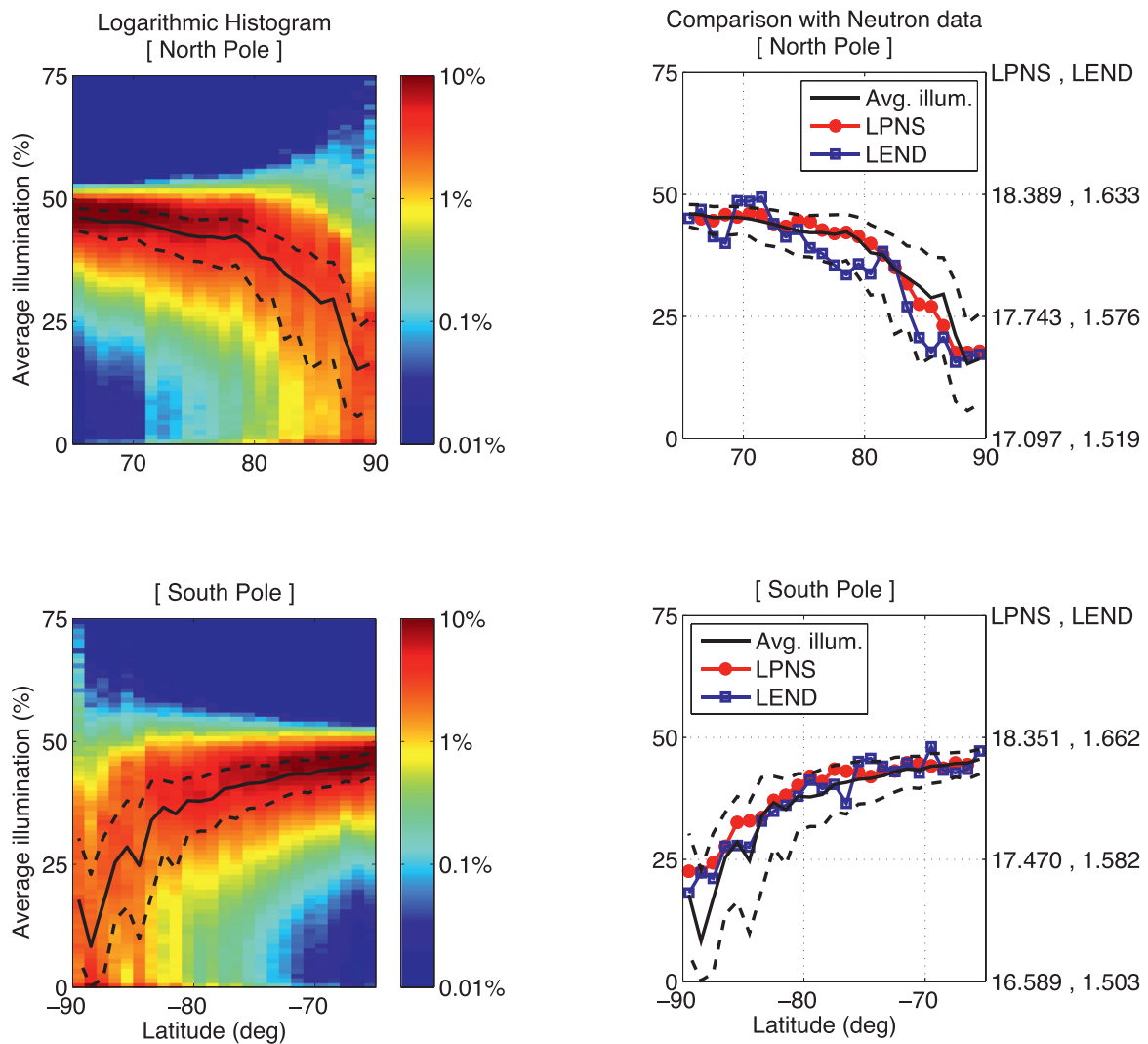


Fig. 15. Histograms of the average illumination in the north (top left) and south (bottom left) polar regions. Each 1°-latitude bin from 65° to the pole is normalized to prevent lower-altitude areas from dominating the count numbers, and highlight the distribution of illumination at each latitude. The color scale is logarithmic. The right panels show the 5°-median 'average illumination' (black), and the corresponding corrected LPNS and LEND epithermal neutron fluxes (Feldman et al., 1998; Mitrofanov et al., 2010). The neutron data were each scaled linearly to fit the average illumination range, as indicated by their corresponding legends. (For interpretation of the references to color in this figure legend, the reader is referred to the web version of this article).

LOLA data were also essential in the detailed documentation of the morphologic transition from complex impact craters, to peak-ring basins, and to multi-ring basins and the morphometric characteristics of these landforms due to their large size and the lack of global high-resolution topography data. Baker et al. (2012) used LOLA data to derive the morphometric characteristics of impact basins on the Moon, assess the trends, and interpret the processes involved in the observed morphologic transitions. Several geometric trends for peak-ring basins have been observed (Fig. 15). A factor of two reduction in the depth to diameter (d/D) ratio in the transition from complex craters to peak-ring basins may be characterized by a steeper trend than known previously. The d/D ratio for peak-ring basins decreases with rim-crest diameter, which may be due to a non-proportional change in excavation cavity growth or scaling, as may occur in the simple to complex transition, or increased magnitude of floor uplift associated with peak-ring formation. Baker et al. (2012) found that new observations of geometric/morphometric properties of protobasins and peak-ring basins place some constraints on the processes that control the onset and formation of interior landforms in peak-ring basins. Comparisons

of the geometric trends of the inner rings of Orientale basin with those of peak-ring basins are generally consistent with a mega-terrace model for the formation of multi-ring basins.

In addition to quantifying the interior structure of impact craters and basins, LOLA data has also been utilized to assess the ejecta deposits and their thickness. Fassett et al. (2011) showed that quantifying the ejecta distribution around large lunar basins is important to understanding the origin of basin rings, the volume of the transient cavity, the depth of sampling, and the nature of the basin formation processes. Fassett et al. (2011) used LOLA altimetry data to estimate the thickness of ejecta in the region surrounding the Orientale impact basin, the youngest and best preserved large basin on the Moon. By measuring the size of craters progressively covered by Orientale ejecta as a function of distance from the basin rim, their measurements yielded ejecta thicknesses of ~2900 m near the Cordillera Mountains, the topographic rim of Orientale, decaying to ~1 km in thickness at a range of 215 km. These measurements imply a volume of ejecta in the region from the Cordillera ring to a radial range of one basin diameter of $\sim 2.9 \times 10^6 \text{ km}^3$.

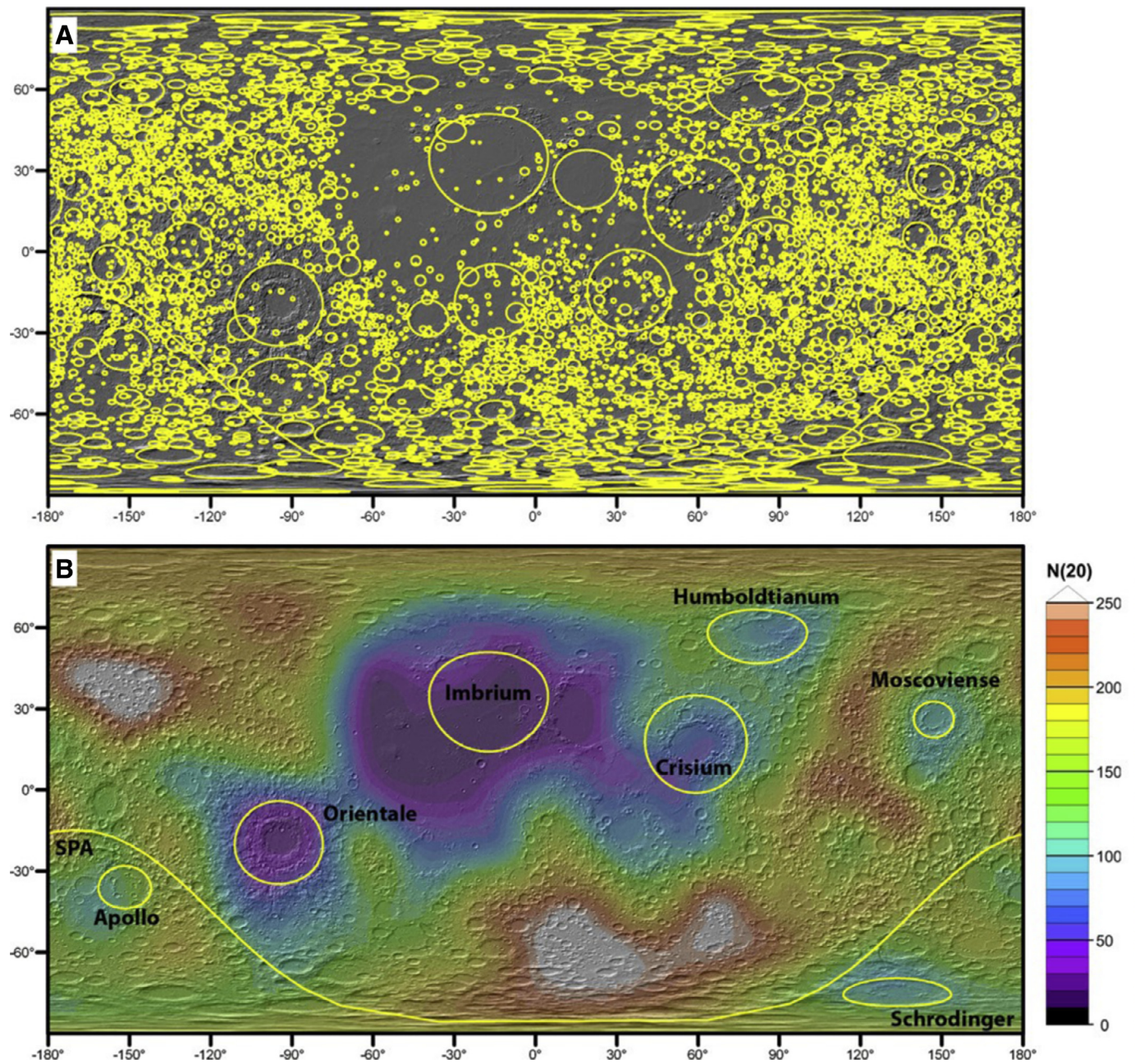


Fig. 16. (A) Outline of craters mapped on the Moon from LOLA data superposed on a hillshade rendering of LOLA topography. (B) Crater densities on the Moon for craters ≥ 20 km in diameter, calculated in a neighborhood of radius 500 km. (Database from Head et al., 2010).

3.6.2. Ages and crater density

LOLA data have provided unprecedented ability and opportunities to assess impact crater location, mapping and density (size-frequency) distributions, and to apply these data to mapping of lunar surface units, and fundamental lunar problems. For example, previous analyses of the global distribution of lunar craters were compiled with images of different resolutions and viewing geometries. The availability of the LOLA altimetry data set permitted the use of a consistent data set that could be illuminated from a variety of perspectives to gain unprecedented views for crater detection and geometry. Using these high-resolution altimetric measurements of the Moon, Head et al. (2010) produced a catalog of all impact craters ≥ 20 km in diameter on the lunar surface (5185 in total) and analyzed their distribution and population characteristics. Fig. 16 shows the outline

of the craters (A) and their density in neighborhoods of 500-km radius. (B).

They found that the most-densely cratered portion of the highlands reached a state of saturation equilibrium. Furthermore, large impact events, such as the Orientale Basin, locally modified the pre-basin crater population to ~ 2 basin radii from the basin center. Important impact basin stratigraphic markers in lunar history, such as Imbrium, Orientale, and Nectaris, are temporally distinguishable on the basis of crater statistics. Finally, the characteristics of pre- and post-mare crater populations support the hypothesis that there were two populations of impactors in early Solar System history and that the transition occurred near the time of the Orientale basin-forming event.

LOLA data also permitted an assessment of the chronology of lunar basins. Impact basin formation is a fundamental process in

the evolution of the Moon and records the history of impactors in the early Solar System. In order to assess the stratigraphy, sequence, and ages of impact basins and the impactor population as a function of time, Fassett et al. (2012) used topography from LOLA to measure the superposed impact crater size–frequency distributions for 30 lunar basins ($D \geq 300$ km). These data generally support the widely used (Wilhelms, 1987) sequence of lunar basins, although Fassett et al. (2012) found significantly higher densities of superposed craters on many lunar basins than derived by Wilhelms (1987) (50% higher densities). Their data also provide new insight into the timing of the transition between distinct crater populations characteristic of ancient and young lunar terrains. On the basis of their data they were able to show that the transition from a lunar impact flux dominated by Population 1 to Population 2 occurred before the mid-Nectarian. This is before the end of the period of rapid cratering, and potentially before the end of the hypothesized Late Heavy Bombardment. LOLA-derived crater densities also suggest that many Pre-Nectarian basins, such as South Pole-Aitken, have been cratered to saturation equilibrium.

3.6.3. Nature, emplacement and history of lunar mare deposits

One of the most fundamental problems in the geological and thermal evolution of the Moon is the nature, modes of emplacement, and duration of lunar mare basalt deposits. LOLA data have been extremely useful in characterizing mare deposits and address related questions. For example, Whitten et al. (2011), using LOLA and Moon Mineralogy Mapper (M3) image and spectral reflectance data, to analyze mare basalt units in and adjacent to the Orientale multi-ring impact basin. They found that mare basalt emplacement on the western nearside limb began prior to the Orientale event as evidenced by the presence of cryptomaria. Whitten et al. (2011) found that the earliest post-Orientale-event mare basalt emplacement occurred in the center of the basin (Mare Orientale) and postdated the formation of the Orientale Basin by about 60–100 Ma. Over the next several hundred million years, they reported that basalt patches were emplaced first along the base of the Outer Rook ring (Lacus Veris) and then along the base of the Cordillera ring (Lacus Autumni), with some overlap in ages. According to Whitten et al. (2011), the latest basalt patches are as young as some of the youngest basalt deposits on the lunar nearside.

A major question in the analysis of the history of the Moon is the role of cryptomaria, ancient volcanic deposits obscured by superposed crater and basin impact ejecta. The timing of cryptomare deposition has implications for the duration and flux of mare basalt volcanism. Whitten and Head (2015a) characterized light plains units on the Moon that might be candidates for cryptomaria. They used LOLA altimetry and roughness data, the presence of dark-halo impact craters associated with a mare basalt mineralogy, and high resolution Moon Mineralogy Mapper (M³) VNIR spectral data to determine cryptomare mineralogy as well as Lunar Prospector (LP) FeO and Th compositional measurements to evaluate which ancient igneous rocks are consistent with the mineralogical observations. Whitten and Head (2015a) observed significant mineralogic variation for a few cryptomaria (e.g., Schiller–Schickard, West Humorum), hinting at heterogeneous mantle source. Of the ancient igneous rocks investigated, Whitten and Head (2015a) found that cryptomare are most consistent with typical mare basalt lithologies, such as low-Ti mare basalts.

Whitten and Head (2015b) used LOLA and related data (M3, LROC, Diviner) to map the global distribution of cryptomaria, in order to provide important information about the thermal and volcanic history of the Moon. In addition, knowing the distribution of cryptomaria can provide information about mantle convection and lunar magma ocean solidification. The global analysis of Whitten and Head (2015b) identified and analyzed the general character-

istics (e.g., topography, surface roughness, rock abundance, albedo, etc.) of lunar light plains in order to better distinguish between ancient volcanic deposits (cryptomaria) and impact basin and crater ejecta deposits. They found 20 discrete regions of cryptomaria, covering approximately 2% of the Moon, which increase the total area covered by mare volcanism to 18% of the lunar surface.

Sori et al. (2016) combined LOLA topography and GRAIL gravity to map the distribution of cryptovolcanic deposits. They modeled potential deposits as buried high-density rectangular prisms and estimated a volume of candidate buried cryptovolcanism between 0.4×10^6 km³ and 4.8×10^6 km³, depending on assumptions about density and crustal compensation state. These deposits have an area between 0.50×10^6 km² and 1.14×10^6 km², which increases the amount of equivalent lunar surface containing volcanic deposits from 16.6% to between 17.9% and 19.5%. The inferred volume of cryptovolcanism is comparable to the smallest estimates of the volume of visible mare basalts and up to ~50% of the largest estimates. GRAIL and LOLA observations thus collectively show that early (pre-3.8 Ga) lunar volcanism is an important element of lunar thermal evolution. Alternatively, the buried material could represent the presence of intrusive Mg-suite sills or plutons.

3.6.4. Floor-fractured craters formation of intrusive structures

LOLA data are critical to the interpretation of modification of craters by mare volcanism and in detecting intrusive bodies, such as sills and the formation of floor fractured craters. For example, floor-fractured craters (FFCs) are a class of lunar craters characterized by anomalously shallow floors cut by radial, concentric, and/or polygonal fractures; additional interior features are moats, ridges, and patches of mare material. Two formation mechanisms have been hypothesized—floor uplift in response to shallow magmatic intrusion and sill formation, and floor shallowing in response to thermally-driven viscous relaxation. Jozwiak et al. (2012) combined LOLA and LROC data to characterize and categorize the population of FFCs and map their distribution on the Moon. They favor formation by shallow magmatic intrusion and sill formation.

In an updated study using LOLA and GRAIL data, Jozwiak et al. (2015) found that the distribution and characteristics of the FFC population correlated strongly with crustal thickness and the predicted frequency distribution of over-pressurization values of magmatic dikes. They found that for a typical nearside lunar crustal thickness, dikes with high over-pressurization values favor surface effusive eruptions, medium values favor intrusion and sill formation, and low values favor formation of solidified dikes concentrated lower in the crust.

3.6.5. Contributions to the geology and surface characteristics of future lunar landing sites

LOLA data helped establish the geological context of potential future landing sites for the United States and other nations. Ivanov et al. (2014) described potential landing sites for the Russian Lunar Glob Mission to the south circumpolar region. The site is located in the southern part of the high topography surrounding the large South Pole–Aitken (SPA) basin. Photogeological analysis of surface LOLA topography and LROC images made it possible to define groups of morphological units (area types): (1) related to the formation of relatively fresh impact craters; (2) associated with larger (>100 km across) degraded craters including external and inner facies; and (3) occupying inter-crater spaces. The comparison of the geological map with the map illustrating the distribution of the epithermal neutrons shows no correlation. The region planned for investigations in the scope of the Luna Glob mission corresponds to the topographic rise of the largest (and, likely, oldest) preserved basin (South Pole–Aitken) and offers a potential op-

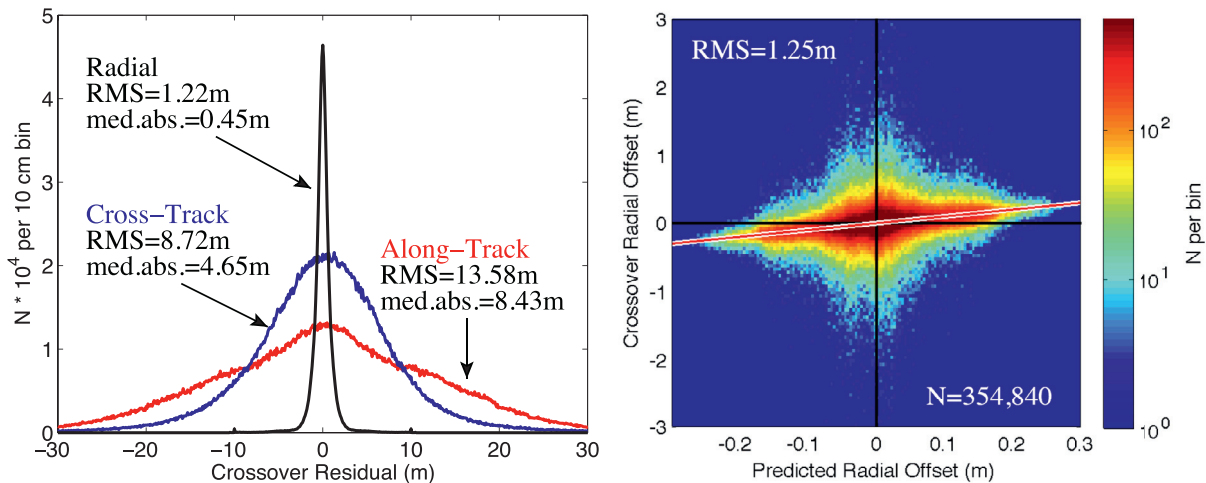


Fig. 17. (Left) Distribution of the adjusted radial, cross-track, and along-track relative track offsets. For clarity, the counts for the cross-track and along-track distributions are multiplied by five. (Right) Two-dimensional histogram of measured and predicted radial offsets (after subtracting the orbital errors estimated by least-squares). The red line is the 1:1 line, not a fit. (After Mazarico et al., 2014). (For interpretation of the references to color in this figure legend, the reader is referred to the web version of this article).

portunity to analyze ancient material lunar crustal materials from depth, and to introduce important constraints into the spectrum of models proposed for explaining the Moon's origin and early evolution.

3.7. Orbit determination and spacecraft positioning

Because of its exploration-driven goals, LRO carried high-resolution instruments, in particular its LROC NAC camera (0.5 m/px), which require accurate knowledge of the spacecraft trajectory in order to combine, compare, and analyze data at a 'landing site' scale. The levied requirement on orbit reconstruction was 50 m (Chin et al., 2007). Unlike most planetary missions, LRO was not tracked by the Deep Space Network (DSN), but rather by a dedicated NASA station at White Sands, NM (with Ka-band downlink for large data volume requirements) with support by worldwide stations of the commercial Universal Space Network (USN) for telemetry and communication. The originally baselined S-band tracking precision was not of sufficient accuracy to achieve the required orbit reconstruction precision, which motivated the addition of a laser ranging experiment (see Section 3.9). However, the station performance was significantly better than expected, both at the White Sands primary station (~0.2–0.3 mm/s Doppler precision, compared to 1 mm/s required) and at the USN sites (~0.4–0.5 mm/s, vs. 3 mm/s). Thus, the radiometric data could ultimately support the original position knowledge goals of the LRO mission. Mazarico et al. (2012) described the orbit determination methodology that enabled the fulfillment of the geodetic requirements. The GEODYN orbit determination and geodetic parameter estimation software, developed and maintained at NASA/GSFC (Pavlis et al., 2013), is used to integrate the spacecraft trajectory, analyze and fit available geodetic measurements. The use of LOLA data through altimetric crossovers was especially important early in the LRO mission to achieve high geodetic accuracy for the LRO orbits and the LOLA ground points, and define the "LOLA geodetic frame" to which the LRO datasets are now controlled. Orbit overlaps better than 20 m were achieved using the LOLA multi-beam crossovers (Mazarico et al., 2012). The development of specially tuned gravity field solutions for LRO (e.g., LLGM-1) made it possible for radio tracking data-only orbit reconstruction to also meet the requirements.

With the advent of the GRAIL mission (Zuber et al., 2013a), the need for crossover-enhanced orbit reconstruction was alleviated, and they now only provide marginal improvements compared to the radio-only solutions (Mazarico et al., 2013). The current orbit solutions produced by the LOLA team and archived on the PDS (<http://geo.pds.nasa.gov/missions/lro/rss.htm>) use the GRGM900C GRAIL gravity field produced at GSFC (Lemoine et al., 2014), truncated at degree and order 600 for computational reasons (and no demonstrated need to include higher terms). The accuracy of these reconstructions is around 10 m in total position and better than 1 m radially. In addition to an overlap analysis, these numbers were assessed from the magnitude of the corrections necessary to align individual LOLA tracks to an existing high-quality LOLA topography model (a crossover adjustment similar to the technique employed in Zuber et al., 2012, and later by Gläser et al., 2014). A study by Wagner et al. (2016, in this issue) of the positions of anthropogenic features on the Moon confirmed this level of orbit quality.

3.8. Detection of the lunar body tide

Because of the gravitational perturbations by the Earth and Sun, the Moon experiences tides over monthly and yearly timescales. The Moon's rigidity yields much smaller time-variable surface deformation than experienced by the Earth under smaller forcing, with a maximum amplitude of ~50 cm (Williams et al., 2011). Two-way lunar laser ranging (LLR) to the corner-cube reflectors brought to the Moon by the Apollo and Lunokhod missions have allowed the precise monitoring of the Moon's orbit and orientation for over 40 years, and the tidal deformation is part of the ranging signal measured (Williams et al., 2008, 2013). The detection of the tidal deformation from orbit is a very challenging measurement, which requires sub-meter accuracies for the spacecraft positioning and altimetric ranges, as well as accurate instrument pointing knowledge or reconstruction (Section 3). However, it can provide an independent measure of the tidal Love number h_2 , largely uncorrelated with the Moon's orbit and inertial orientation.

Mazarico et al. (2014) considered more than 5 billion measurements acquired in the low-altitude, circular LRO orbit (prior to December 2011), from which > 500,000 multi-beam crossover measurements were selected for co-registration. The relative adjustments required to co-align the track pairs were then utilized

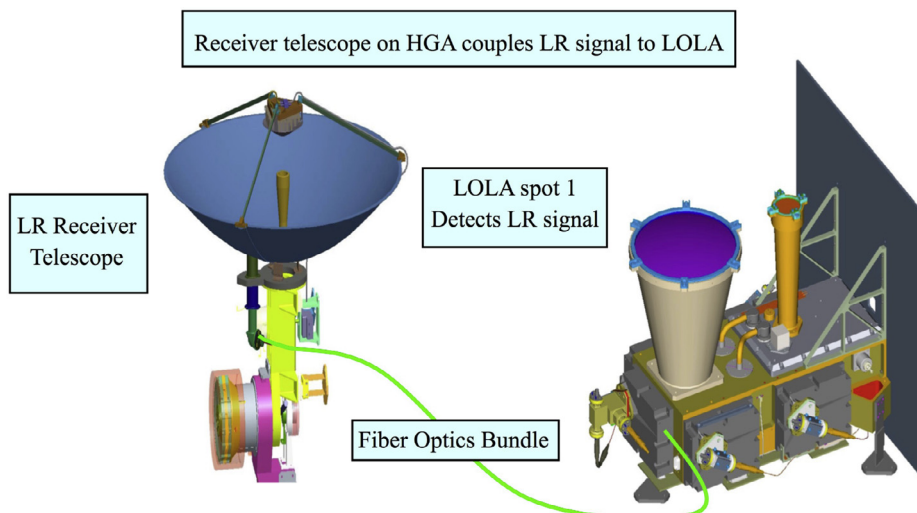


Fig. 18. Schematic of the LRO laser ranging (LR) system. The Earth uplink signal is detected by the LR telescope mounted on the HGA, and sent to LOLA channel 1 for processing via the fiber optic bundle. Adapted from Zuber et al. (2010).

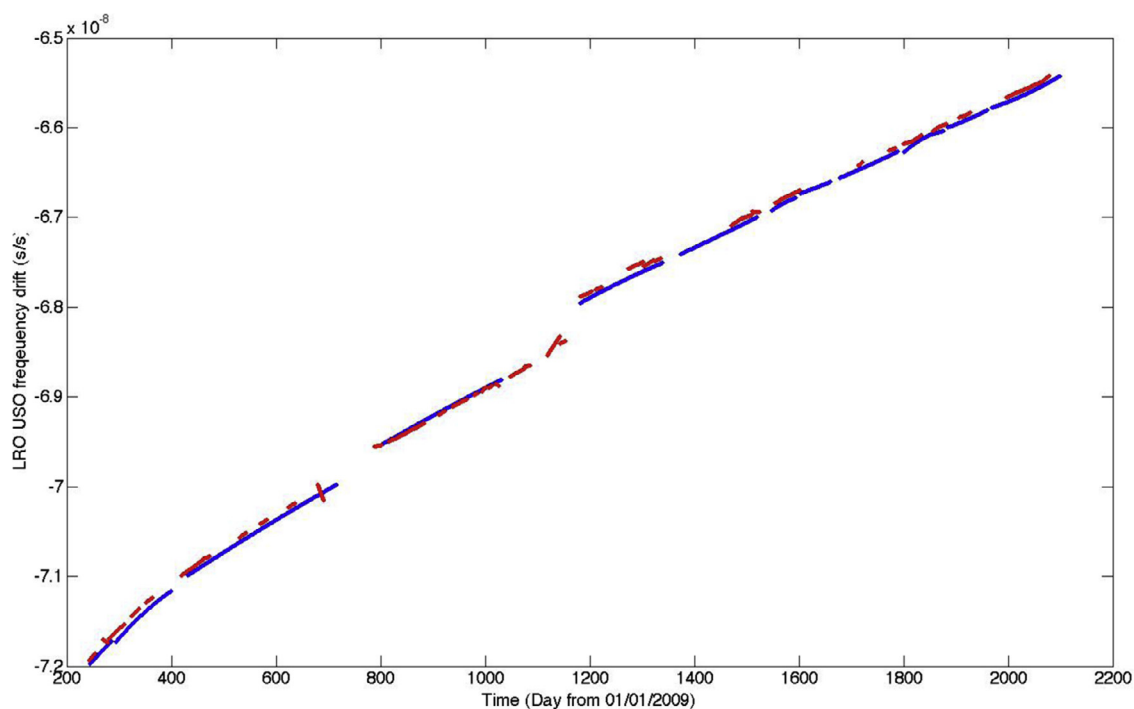


Fig. 19. LRO USO drift estimated by NGSRLR LR data over several months (in blue) and by GEODYN processing with all LR data over two-week arcs converged with GRAIL gravity (GRGM900C, in red). (For interpretation of the references to color in this figure legend, the reader is referred to the web version of this article).

in a weighted least-squares filter, which jointly estimated the tidal Love number h_2 and additional spacecraft orbit and instrument pointing errors (Section 3). Fig. 17 shows the distribution of radial, cross-track, and along-track offsets.

The LOLA-derived value of $h_2 = 0.0371 \pm 0.0033$, and is compatible with LLR-derived values ($h_2 = 0.03786 \pm 0.0076$, Williams et al., 2008). Other values predicted based on GRAIL-derived interior models result in larger values ($h_2 \sim 0.0423$, Williams et al., 2014; $h_2 = 0.0476 \pm 0.0064$, Williams et al., 2013).

The detection of the lunar body tide from orbit with LOLA data shows the capabilities of laser altimeters for key geophysical objectives, which can be important for other bodies (Steinbrügge et al., 2015; Mazarico et al., 2015). Further studies of the LOLA data may enable the first estimates of tidal distortion, which could for

example help determine if the viscosity beneath the Procellarum KREEP Terrain (PKT) region is reduced due to a thermal anomaly (Wieczorek et al., 2006), and distinguish h_{20} from h_{21} and h_{22} .

3.9. Laser ranging

In order to improve Precision Orbit Determination (POD) of the LRO spacecraft, a Laser Ranging (LR) experiment was added to the LRO mission during development (Zuber et al., 2010). Mao et al. (2016) describe in detail the LR experiment as well as the time-keeping and geodetic results.

The goal of LR was to perform one-way time-of-flight measurements from Earth-based satellite laser ranging stations to LRO. Laser pulses from the Earth were received by the LR telescope (LRT, Ramos-Izquierdo et al., 2009), mounted on and co-bore-sighted

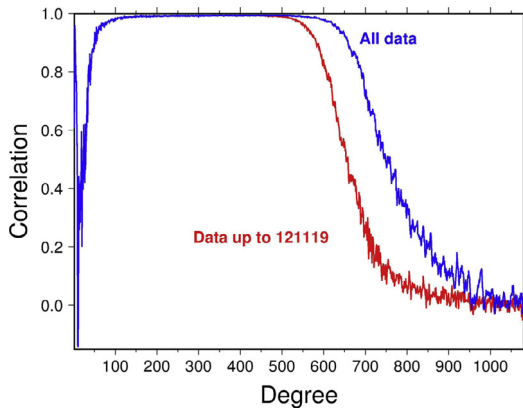


Fig. 20. Correlation between GRAIL free-air gravity and gravity derived from LOLA topography assuming a density of 2550 kg m^{-3} . The blue curve shows the correlation of a gravity field obtained from data up to November 9, 2012 and the red curve shows the correlation including the last month of low-altitude GRAIL data acquired prior to the spacecraft planned lunar impacts. (For interpretation of the references to color in this figure legend, the reader is referred to the web version of this article).

with the LRO High Gain Antenna (HGA). The LRT pointed at the Earth through a 3.81-cm diameter, off-center hole in the primary reflector of the HGA. With a 30-mrad ($\sim 1.7^\circ$) field of view and a 19-mm diameter aperture, the LRT field of view covered nearly the entire Earth. The laser pulses intercepted by the LRT were transmitted via a ~ 10 -m multi-fiber-optic cable at the focal point of the LRT attached to the HGA running to the LOLA channel 1 detector as shown in Fig. 18. The LOLA channel-1 detector was designed to receive both the 1064-nm lunar return signals and the 532-nm Earth signals via two separate range windows within the 35.7-ms LOLA measurement cycle.

NASA's the Next Generation Satellite Laser Ranging (NGSLR) station at Greenbelt, Maryland, was the primary LRO-LR ground station. NGSLR was modified from its original design of performing two-way laser ranging to the retro-reflectors on Earth-orbiting satellites to enable tracking of both LRO and Earth-orbiting satellites. A sub-network of 9 SLR stations (McDonald, Texas, USA; Monument Peak, California, USA; Yarragadee, Australia; Hartbeesthoek, South Africa; Greenbelt in Maryland, USA; Zimmerwald, Switzerland; Wettzell, Germany; Herstmonceux, England; Grasse, France) of the International Laser Ranging Service (ILRS) (Pearlman et al., 2007) provided global coverage for LRO-LR. The tracking sites were equipped with Rubidium (Rb), Cesium (Cs) or Hydrogen-maser clocks to maintain a stable time base. Near-real time (within 30 s) tracking feedback was provided to the sites to allow adjustment of their laser fire times and angular biases to mitigate orbit prediction errors. The LR station network demonstrated that close to 24-h per day tracking coverage was possible for ranging to LRO.

Two methods were used to independently estimate the long term drift of the LRO Ultra-stable Oscillator (USO). One method directly compares the LOLA receive MET times with the laser transmit times in UTC from main LR station NGSLR over a two to three-month time span during which there are no clock breaks at either NGSLR or LRO. The USO frequency drift and aging are obtained by removing the calculated light time from the out-going and received time difference and fitting a quadratic function to the residuals. The resulting USO drift is shown in the Fig. 19 in blue. Another method estimates the LRO USO frequency and aging in the orbit determination process using the GEODYN program. The GEODYN estimated USO drift values, plotted in Fig. 19 in red, agree well with those from the direct transmit-receive time comparison.

Given appropriate clock synchronization (Bauer et al., 2016a), the LR observations have been demonstrated to improve LRO or-

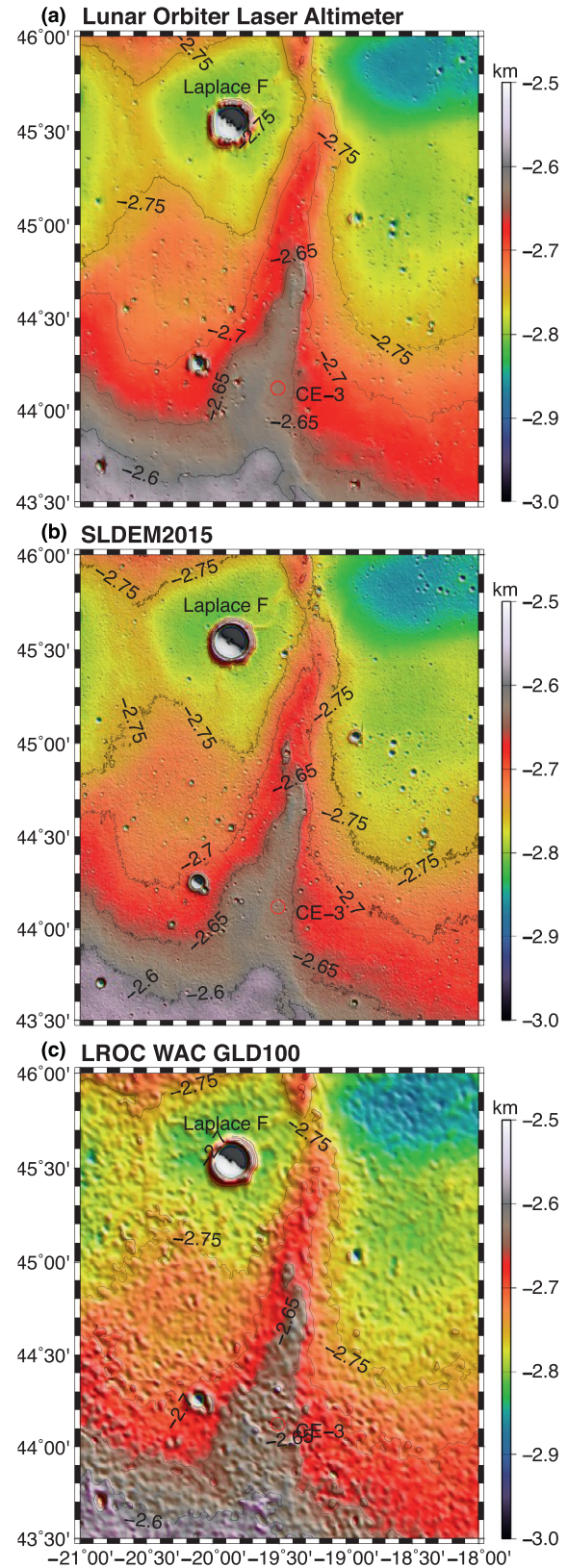


Fig. 21. Comparison of DEMs of the Chang'E 3 landing site (labeled red circle) in Mercator projection. (a) LOLA DEM with continuous curvature interpolation to fill gaps between tracks; (b) SLDEM2015, a lunar topographic model made from a combination of LOLA topography SELENE Terrain Camera (TC) images; and (c) LROC WAC GLD100 DEM. (For interpretation of the references to color in this figure legend, the reader is referred to the web version of this article).

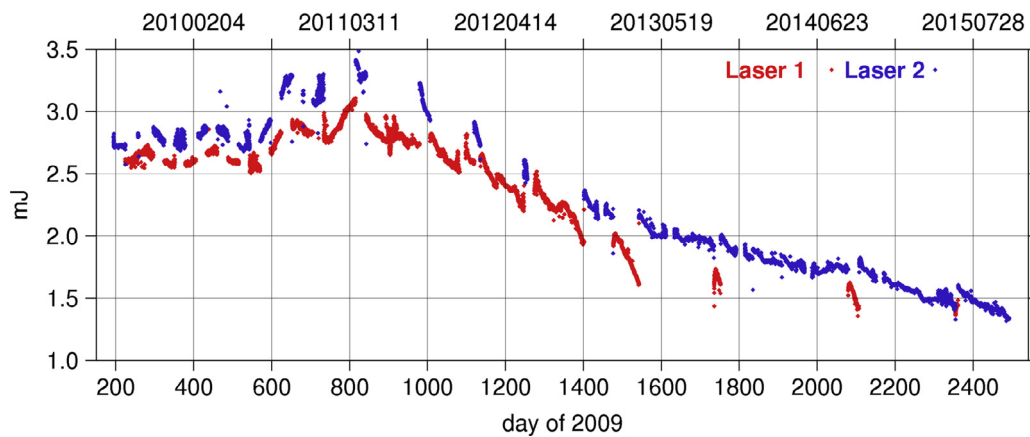


Fig. A1. History of output energy from laser 1 and laser 2 as measured by the laser energy monitor.

Table 3

Area in permanent shadow (km²) based on illumination simulations with maps of varying resolution and topographic coverage density.

North	Mazarico et al. (2011), 240 m/px	Updated LOLA map, 240 m/px	Updated LOLA map, 120 m/px	Updated LOLA map, 60 m/px	Updated LOLA map, 20 m/px
>82.5°N	9670	10,894	12,335	13,662	–
>85°N	5088	5609	6365	7025	–
>87.5°N	1811	1929	2137	2305	2830
>89°N	321	349	381	409	501
>82.5°S	12,491	13,217	14,180	15,374	–
>85°S	7106	7377	7774	8260	–
>87.5°S	3668	3735	3827	3928	4401
>89°S	428	441	463	488	572

bits, by a factor of two or better for arc overlaps (Bauer et al., 2016b).

3.10. Synergy with gravity from the GRAIL mission

While the LRO mission was in operation in lunar orbit, the GRAIL mission (Zuber et al., 2013a) to the Moon was launched to obtain a high-resolution gravity of the Moon. The twin GRAIL spacecraft acquired accurate satellite-to-satellite range-rate data (0.03–0.05 $\mu\text{m/s}$ precision over 1–2 s), which ultimately yielded an unprecedented resolution measure of the lunar gravity field (Zuber et al., 2013b; Konopliv et al., 2013; Lemoine et al., 2013, 2014). One of the first scientific results from GRAIL was a spherical harmonic gravity solution that, when compared with the LOLA spherical harmonic model of topography, showed agreement at the 99% level in the degree band 120 to 600. Fig. 20 shows the correlation between the gravity and topography. This high correlation indicates that lunar gravity at those scales is primarily the result of the topography, which can be explained by extensive fracturing of the lunar crust that homogenized density variations in response to impact bombardment, particularly in early lunar history (Zuber et al., 2013b).

3.11. LOLA+TC combined topographic model

The ability of laser altimeters to obtain global measurements independent of solar illumination conditions provides an advantage over passive stereoscopic imaging, particularly at high latitudes (>60°) where such imaging is hindered by low solar incidence angles, shadowing and permanent shadow. In addition, laser altimetry provides a more accurate geodetic framework to which stereo models can be controlled. On the other hand, stereo imaging can provide denser surface coverage than laser altimetry, especially near the equator. Gaps in the LOLA coverage as wide as a few kilometers still persist near the equator, due to the very narrow cross-

track width of the individual LOLA profiles (~50 m). Thus, the LOLA altimetric dataset can benefit from the extensive cross-track coverage provided by camera data, such as the SELENE Terrain Camera (TC) imagery. The TC was a push-broom stereo imager onboard the Kaguya spacecraft (Haruyama et al., 2008) that acquired stereo imaging with individual ~30 km-wide swaths, and covered over 99% of the lunar surface with a spatial posting of 10 m.

Barker et al. (2016a) presented a method for co-registering the TC data to the latest, most accurate GRAIL gravity-derived LOLA geodetic framework, yielding 3–4 m RMS elevation residuals to LOLA profiles and increasing the fraction of residuals < 5 m from ~50% prior to registration, to ~90% after registration. By combining both datasets, gaps in the LOLA data could be filled without the need for interpolation during map production. The resulting DEM, designated as SLDEM2015, covers latitudes between $\pm 60^\circ$ with a horizontal resolution of 512 pppd, and is available from the Planetary Data System LOLA data node (<http://imbrium.mit.edu/DATA/SLDEM2015/>).

The SLDEM2015 fills an important part of the resolution/coverage/accuracy parameter space that previously was unoccupied by most other commonly-used lunar DEMs. For example, the LROC WAC GLD100 covers latitudes within $\pm 79^\circ$ with an effective horizontal resolution ~1 km and a mean vertical accuracy ~10–20 m (Scholten et al., 2012). The LROC NAC provides higher-resolution stereo DEMs (pixel scale ~2–5 m), but NAC stereo imagery covers only ~2% of the surface (Henriksen et al. (2016)). Therefore, with a ~3–4 m accuracy and ~60 m resolution covering ~87% of the surface, the SLDEM2015 has many geophysical, geological, and cartographic applications in lunar science, as well as exploration and mission design. Studies requiring the high geodetic accuracy of the LOLA data and the excellent spatial coverage of the TC data will especially benefit. In particular, it will improve the orthorectification and co-registration of diverse lunar datasets to the latest LRO/LOLA/GRAIL geodetic system by avoiding the gaps nor-

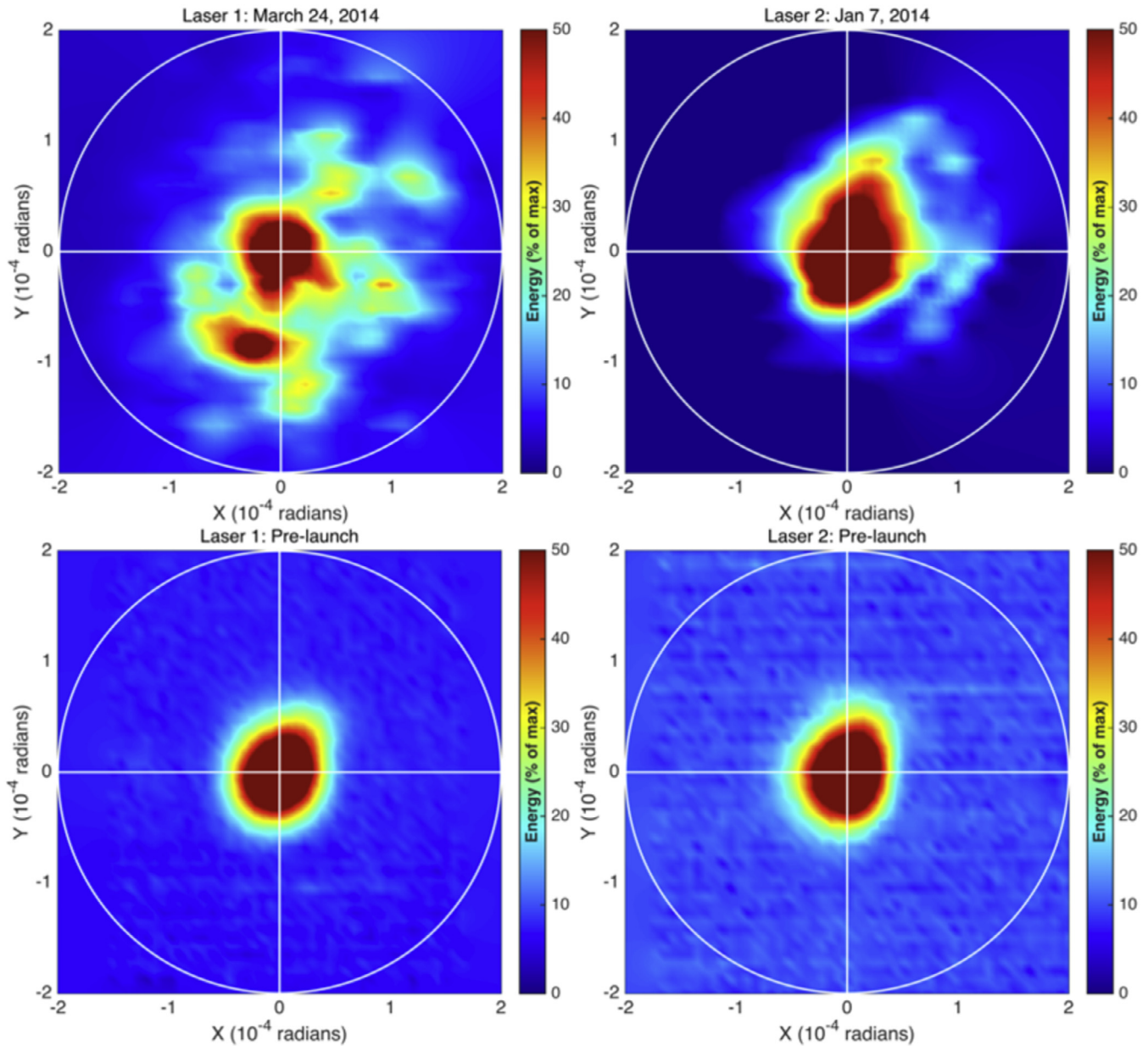


Fig. A2. Far-field patterns of both lasers measured prior to launch (bottom) and reconstructed from active Earth scans ~ 5 years subsequent to launch (top). The white circle is the receiver field-of-view.

mally present between LOLA groundtracks. A comparison of these three DEMs is shown in Fig. 21.

4. Summary/conclusions

The Lunar Orbiter Laser Altimeter will continue to acquire altimetry over the Moon during the LRO extended missions, as well as roughness and albedo data. As detailed herein, the results of mapping to date have demonstrably contributed towards site characterization and geodetic positioning required for future exploration. The LOLA data will benefit all manner of analyses to advance understanding of lunar science. Knowledge of topography, slopes, roughness, and reflectance bear on numerous outstanding problems in lunar geology and geophysics, and LOLA has, to this point, provided the highest resolution and highest accuracy topographic model for any solid planetary body in the Solar System.

Acknowledgments

We would like to acknowledge the LOLA Engineering Team for the design and development of an outstanding instrument. We also recognize the support of the Lunar Reconnaissance Orbiter spacecraft and operations teams, and the Project Science Office without whom the LOLA investigation would not have been possible. In addition, we gratefully acknowledge the contributions of Mikhail A. Kreslavsky, Caleb Fassett, Debra Hurwitz and Lauren Jozwiak toward making LOLA a success through their scientific utilization of the data to address important scientific problems.

Appendix: Instrument. changes over time

Immediately after the turn-on of LOLA, it was evident that the instrument had an optical alignment problem when the space-

Table A1
LOLA instrument performance.

Measurement	LOLA performance, rms
Altimetry	10 cm
Radiometry, active	3%, after calibration
Radiometry, passive	5%, after calibration
Surface roughness	1.0 m, 5 m spot
Slopes	0.5 m, 25 m baseline
	0.3 deg, 25 m baseline
	0.1 deg, 100 m baseline

craft passed from the sunlit side of the Moon to the dark side. It was subsequently recreated in the laboratory that the beam expander (transmitter telescope) and the receiver telescope were being pulled out of alignment due to the contraction of the thermal blanket that protects the instrument. All the spots were affected when over the nighttime lunar surface, thus reducing the quantity of data acquired, but they quickly returned to proper alignment as soon as sunlight reached the spacecraft. Because of the specific direction and magnitude of the movement of the beams relative to the detectors, two out of the five spots became aligned with different receiver channels and could yield altimetric measurements over the dark side. This effect has generally been referred to as the “LOLA thermal blanket anomaly” and has persisted throughout the mission.

As the laser output power decreased over time, the performance of the instrument has slowly deteriorated, limiting the maximum range to which LOLA could obtain an adequate return signal. LOLA has 2 laser transmitters, and both have shown similar decrease in output, although Laser 1 has decayed more rapidly than Laser 2. At the present time, Laser 2 is the operational laser of choice. Both lasers were designed for 1 billion pulses (shots) and both lasers have emitted over 2 billion pulses. The output of the two lasers since launch is shown in Fig. A1. In late 2010, the energy of both lasers appeared to increase, however this is believed to be an artifact of the laser energy monitor systems. At the same time, the energy measured at the receiver, corrected for distance to the surface and surface reflectivity, began to decline. The received energy also drops sharply during the twice-yearly transition through a solar beta angle of 90 degrees, where the spacecraft constantly faces the relatively cold lunar terminator.

From early in the mission, the experiments measured a thermally driven pointing anomaly, when LOLA is facing deep space or the cold side of the Moon. Averaging all 3 successful active Earth scans for all 5 spots and both lasers, the downlink data indicate a nighttime offset from the nominal boresight of $\Delta X = 63 \pm 35 \mu\text{rad}$ and $\Delta Y = -351 \pm 57 \mu\text{rad}$ in the along-track and cross-track directions, respectively.

The downlink data also allowed reconstruction of the laser far-field pattern (Fig. A2). The primary lobe beam width has not changed significantly from the pre-flight value of $100 \mu\text{rad}$, but there is more energy spread among sidelobes, outside the primary lobe, than in the pre-flight tests. The far-field pattern of Laser 1 is more dispersed and irregular than that of Laser 2. The uplink data indicate an average nighttime receiver boresight correction of $\Delta X = 0 \pm 71 \mu\text{rad}$ and $\Delta Y = 140 \pm 28 \mu\text{rad}$, possibly caused by the thermal blanket pulling on the receiver telescope. Comparing data from such experiments shortly after launch and nearly 5 years later allows the direct measurement of changes in the laser characteristics and provides critical data to understand the laser behavior and refine the instrument calibration.

Table 3, Table A1

References

- Araki, H., Tazawa, S., Noda, H., et al., 2009. Lunar global shape and polar topography derived from Kaguya-LALT laser altimetry. *Science* 323, 897–900. doi:10.1126/science.1164146.
- Bandfield, J.L., Hayne, P.O., Williams, J.-P., et al., 2015. Lunar surface roughness derived from LRO diviner radiometer observations. *Icarus* 248, 357–372. doi:10.1016/j.icarus.2014.11.009.
- Baker, D.M.H., Head III, J.W., Fassett, C.I., et al., 2011. The transition from complex crater to peak-ring basin on the Moon: New observations from the Lunar Orbiter Laser Altimeter (LOLA) instrument. *Icarus* 214, 377–393. doi:10.1016/j.icarus.2011.05.030.
- Baker, D.M.H., Head III, J.W., Neumann, G.A., et al., 2012. The transition from complex craters to multi-ringed basins on the Moon: Quantitative geometric properties from Lunar Reconnaissance Orbiter Lunar Orbiter Laser Altimeter (LOLA) data. *J. Geophys. Res.* 117, E00H16. doi:10.1029/2011JE004021.
- Barker, M.K., Mazarico, E., Neumann, G.A., et al., 2016a. A new lunar digital elevation model from the lunar orbiter laser altimeter and SELENE terrain camera. *Icarus* <http://dx.doi.org/10.1016/j.icarus.2015.07.039>.
- Barker, M.K., Sun, X., Mazarico, E., et al., 2016b. Lunar phase function at 1064 nm from lunar orbiter laser altimeter passive and active radiometry. *Icarus* <http://dx.doi.org/10.1016/j.icarus.2016.02.008>.
- Bauer, S., Hussman, H., Oberst, J., et al., 2016a. Processing of one-way laser ranging data to LRO: Performance and calibration of spacecraft and ground station clocks. (Submitted for publication). *Icarus*.
- Bauer, S., Oberst, J., Dirkx, D., et al., 2016b. Demonstration of orbit determination for the Lunar Reconnaissance Orbiter using one-way laser ranging data. *Planet. Space Sci.* (Submitted for publication).
- Besse, S., Yohota, Y., Boardman, J., et al., 2013. One Moon, many measurements 2: Photometric corrections. *Icarus* 226, 127–139. doi:10.1016/j.icarus.2013.05.009.
- Bussey, D.B.J., Spudis, P.D., Robinson, M.S., 1999. Illumination conditions at the lunar South Pole. *Geophys. Res. Lett.* 26, 1187–1190. doi:10.1029/1999GL000213.
- Campbell, D.B., Campbell, B.A., Carter, L.M., et al., 2006. No evidence for thick deposits of ice at the lunar south pole. *Nature* 443, 835–837. doi:10.1038/nature05167.
- Chin, G., Brylow, S., Foote, M., et al., 2007. Lunar reconnaissance orbiter overview: The instrument suite and mission. *Space Sci. Rev.* 129, 391–419. doi:10.1007/s11214-007-9153-y.
- Clark, R.N., 2009. Detection of adsorbed water and hydroxyl on the Moon. *Science* 326, 562–564. doi:10.1126/science.1178105.
- Farrell, W.M., Hurley, D.M., Zimmerman, M.I., 2015. Solar wind implantation into lunar regolith: Hydrogen retention in a surface with defects. *Icarus* 255, 116–126. doi:10.1016/j.icarus.2014.09.014.
- Fassett, C.I., Thomson, B.J., 2014. Crater degradation on the lunar maria: Topographic diffusion and the rate of erosion on the Moon. *J. Geophys. Res.* 119, 2255–2271. doi:10.1002/2014JE004698.
- Fassett, C.I., Head III, J.W., Kadish, S.J., et al., 2012. Lunar impact basins: Stratigraphy, sequence and ages from superposed impact crater populations measured from Lunar Orbiter Laser Altimeter (LOLA) data. *J. Geophys. Res.* 117, E00H06. doi:10.1029/2011JE003951.
- Fassett, C.I., Head III, J.W., Smith, D.E., et al., 2011. Thickness of proximal ejecta from the Orientale Basin from Lunar Orbiter Laser Altimeter (LOLA) data: Implications for multi-ring basin formation. *Geophys. Res. Lett.* 38, L17201. doi:10.1029/2011GL048502.
- Feldman, W.C., Barraclough, B.L., Maurice, S., et al., 1998. Major compositional units of the Moon: Lunar prospector thermals and fast neutrons. *Science* 281, 1483–1493.
- Garrick-Bethell, I., Perera, V., Nimmo, F., et al., 2014. The tidal-rotational shape of the Moon and evidence for polar wander. *Nature* doi:10.1038/nature13639.
- Gladstone, G.R., Retherford, K., Egan, E., et al., 2012. Far-ultraviolet reflectance properties of the Moon's permanently shadowed regions. *J. Geophys. Res.* 117, E00H04. doi:10.1029/2011JE003913.
- Gläser, P., Scholten, F., De Rosa, D., et al., 2014. Illumination conditions at the lunar south pole using high resolution digital terrain models from LOLA. *Icarus* 243, 78–90. doi:10.1016/j.icarus.2014.08.013.
- Hapke, B., Denevi, B., Sato, H., et al., 2012a. The wavelength dependence of the lunar phase curve as seen by the lunar reconnaissance orbiter wide-angle camera. *J. Geophys. Res.* 117, 0. doi:10.1029/2011JE003916.
- Hapke, B., 2012b. *Theory of Reflectance and Emittance Spectroscopy, second ed.* Cambridge University Press, Cambridge.
- Haryuama, J., Matsunaga, T., Ohtake, M., et al., 2008. Global lunar-surface mapping experiment using the lunar imager/spectrometer on SELENE. *Earth Planets Space* 60, 243–255. doi:10.1186/BF03352788.
- Head III, J.W., Fassett, C.I., Kadish, S.J., et al., 2010. Global distribution of large lunar craters: Implications for resurfacing and impactor populations. *Science* 329, 1504–1507.
- Hemingway, D.J., Garrick-Bethell, I., Kreslavsky, M.A., 2015. Latitudinal variation in spectral properties of the lunar maria and implications for space weathering. *Icarus* 261, 66–79. doi:10.1016/j.icarus.2015.08.004.
- Henriksen, M.R., Manheim, M.R., Speyerer, E.J., et al., 2016. Extracting accurate and precise topography from LROC narrow angle camera stereo observations. (in this issue). *Icarus*.

- Ivanov, M.A., Abdrakhimov, A.M., Basilevsky, A.T., et al., 2014. Geological context of the potential landing site of the luna-glob mission. *Sol. Syst. Res.* 48, 391–402. Russian: *Astronomicheskii Vestnik* 48, 423–435, doi: 10.7868/S0320930X14060024. doi: 10.1134/S0038094614060021.
- Jozwiak, L.M., Head III, J.W., Zuber, M.T., et al., 2012. Lunar floor-fractured craters: Classification, distribution, origin and implications for magmatism and shallow crustal structure. *J. Geophys. Res.* 117, E11005. doi: 10.1029/2012JE004134.
- Jozwiak, L.M., Head III, J.W., Wilson, L., 2015. Lunar floor-fractured craters as magmatic intrusions: Geometry, modes of emplacement, associated tectonic and volcanic features, and implications for gravity anomalies. *Icarus* 248, 424–447. doi: 10.1016/j.icarus.2014.10.052.
- Kalynn, J., Johnson, C.L., Osinski, G.R., et al., 2013. Topographic characterization of lunar complex craters. *Geophys. Res. Lett.* 40, 38–42. doi: 10.1029/2012GL053608.
- Keane, J.T., Matsuyama, I., 2014. Evidence for lunar true polar wander and a past low-eccentricity, synchronous lunar orbit. *Geophys. Res. Lett.* 41, 6610–6619. doi: 10.1002/2014GL061195.
- Konopliv, A.S., Park, R.S., Yuan, D.-N., et al., 2013. The JPL lunar gravity field to spherical harmonic degree 660 from the GRAIL primary mission. *J. Geophys. Res.* 118, 1–20. doi: 10.1002/jgre.20097.
- Kreslavsky, M.A., Head III, J.W., 2012. New observational evidence of strong seismic effects of basin-forming impacts on the Moon from Lunar reconnaissance orbiter laser altimeter data. *J. Geophys. Res.* 117, E00H24. doi: 10.1029/2011JE003975.
- Kreslavsky, M.A., Head III, J.W., Neumann, G.A., et al., 2013. Lunar topographic roughness maps from Lunar Orbiter Laser Altimeter (LOLA) data: Scale dependence and correlation with geologic features and units. *Icarus* 226, 52–66. doi: 10.1016/j.icarus.2013.04.027.
- Lemelin, M., Lucey, P.G., Neumann, G.A., et al., 2016. Improved calibration of reflectance data from the LRO Lunar Orbiter Laser Altimeter (LOLA) and implications for space weathering. *Icarus* 273, 315–328. doi: 10.1016/j.icarus.2016.02.006.
- Lemoine, F.G., Goossens, S., Sabaka, T.J., et al., 2013. High-degree gravity models from GRAIL primary mission data. *J. Geophys. Res.* 118, 1676–1698. doi: 10.1002/jgre.
- Lemoine, F.G., Goossens, S., Sabaka, T.J., et al., 2014. GRGM900C: A degree 900 lunar gravity model from GRAIL primary and extended mission data. *Geophys. Res. Lett.* 41, 3382–3389. doi: 10.1002/2014GL060027.
- Lucey, P.G., Neumann, G.A., Riner, M.A., et al., 2014. The Global Albedo of the Moon at 1064-nm from the Lunar Orbiter Laser Altimeter (LOLA). *J. Geophys. Res.* 119, 1665–1679. doi: 10.1002/2013JE004592.
- Mao, D., McGarry, J.F., Mazarico, E., et al., 2016. The laser ranging experiment of the lunar reconnaissance orbiter: Five years of operations and data analysis. (in this issue). *Icarus*.
- Margot, J.-L., Campbell, D.B., Jurgens, R.F., et al., 1999. Topography of the lunar poles from radar interferometry: A survey of cold trap locations. *Science* 284, 1658–1660. doi: 10.1126/science.284.5420.1658.
- Mazarico, E., Neumann, G.A., Smith, D.E., et al., 2011a. Illumination conditions of the lunar polar regions using LOLA topography. *Icarus* 211, 1066–1081. doi: 10.1016/j.icarus.2010.10.030.
- Mazarico, E., Neumann, G.A., Smith, D.E., et al., 2011b. Illumination conditions of the lunar poles to 65 degrees latitude from lunar orbiter laser altimeter data. In: *Annual Meeting of the Lunar Exploration Analysis Group. Houston, Texas Abstract #51.*
- Mazarico, E., Rowlands, D.D., Neumann, G.A., et al., 2012. Orbit determination of the lunar reconnaissance orbiter. *J. Geod.* 86 (3), 193–207. doi: 10.1007/s00190-011-0509-4.
- Mazarico, E., Lemoine, F.G., Goossens, S.J., et al., 2013. Improved precision orbit determination of lunar orbiters from the GRAIL-derived lunar gravity models. In: *23rd AAS/AIAA Space Flight Mechanics Meeting. AAS. Hawaii, Kauai, pp. 13–274.*
- Mazarico, E., Barker, M.K., Neumann, G.A., et al., 2014. Detection of the lunar body tide by the lunar orbiter laser altimeter. *Geophys. Res. Lett.* 41, 2282–2288. doi: 10.1002/2013GL059085.
- Mazarico, E., Genova, A., Neumann, G.A., et al., 2015. Simulated recovery of Europa's global shape and tidal Love numbers from altimetry and radio tracking during a dedicated flyby tour. *Geophys. Res. Lett.* 42, 3166–3173. doi: 10.1002/2015GL063224.
- McClanahan, T.P., Mitrofanov, I.G., Boynton, W.V., et al., 2015. Evidence for the sequestration of hydrogen-bearing volatiles towards the Moon's southern pole-facing slopes. *Icarus* 255, 88–99. doi: 10.1016/j.icarus.2014.10.001.
- McGovern, J.A., Bussey, D.B., Greenhagen, B.T., et al., 2013. Mapping and characterization of non-polar permanent shadows on the lunar surface. *Icarus* 223, 566–581. doi: 10.1016/j.icarus.2012.10.018.
- Mitrofanov, I.G., Sanin, A.B., Boynton, W.V., et al., 2010. Hydrogen mapping of the lunar south pole using the LRO neutron detector experiment LEND. *Science* 330, 483–486. doi: 10.1126/science.1185696.
- Neumann, G.A., Cavanaugh, J.F., Sun, X., et al., 2013. Bright and dark polar deposits on Mercury: Evidence for surface volatiles. *Science* 339, 296–300. doi: 10.1126/science.1229764.
- Neumann, G.A., Zuber, M.T., Wieczorek, M.A., et al., 2015. Lunar impact basins revealed by gravity recovery and interior laboratory measurements. *Sci. Adv.* 1, 0852. doi: 10.1126/sciadv.1500852.
- Noda, H., Araki, H., Goossens, S., et al., 2008. Illumination conditions at the lunar polar regions by KAGUYA, SELENE laser altimeter. *Geophys. Res. Lett.* 35, L24203. doi: 10.1029/2008GL035629.
- Nozette, S., Spudis, P.D., Robinson, M.S., et al., 2001. Integration of lunar polar remote-sensing data sets: evidence for ice at the lunar south pole. *J. Geophys. Res.* 106 (E10), 23253–23266.
- Pavlis, D.E., J. Wimert, and J.J. McCarthy, 2013. GEODYN II System Description, vol. 1–5, contractor report, SGT Inc., Greenbelt, Md.
- Pearlman, M., Noll, C., Gurtner, W., et al., 2007. *The International Laser Ranging Service and its support for GGOS - monitoring and understanding a dynamic planet with geodetic and oceanographic tools.* Tregoning and Rizos, pp. 741–748.
- Pieters, C.M., Goswami, J.N., Clark, R.N., et al., 2009. Character and spatial distribution of OH/H₂O on the surface of the Moon seen by M3 on Chandrayaan-1. *Science* 326, 568–572. doi: 10.1126/science.1178658.
- Ramos-Izquierdo, L., Stanley Scott III, V., Connelly, J., et al., 2009. Optical system design and integration of the lunar orbiter laser altimeter. *Appl. Opt.* 48, 3035–3049.
- Robinson, M.S., Brylow, S.M., Tschimmel, M., et al., 2009. Lunar Reconnaissance Orbiter Camera (LROC) instrument overview. *Space Sci. Rev.* 150, 81–124. doi: 10.1007/s11214-010-9634-2.
- Rosenburg, M.A., Aharonson, O., Head, J.W., et al., 2011. Global surface slopes and roughness of the Moon from the lunar orbiter laser altimeter. *J. Geophys. Res.* 116, E02001. doi: 10.1029/2010JE003716.
- Rosenburg, M.A., Aharonson, O., Sari, R., 2015. Topographic power spectra of cratered terrains: Theory and application to the Moon. *J. Geophys. Res.* 120, 177–194. doi: 10.1002/2014JE004746.
- Sato, H., Robinson, M.S., Hapke, B., et al., 2014. Resolved Hapke parameter maps of the Moon. *J. Geophys. Res.* 119, 1775–1805. doi: 10.1002/2013JE004580.
- Scholten, F., Oberst, J., Matz, K.-D., et al., 2012. GLD100: The near-global lunar 100 m raster DTM from LROC WAC stereo image data. *J. Geophys. Res.* 117, 0. doi: 10.1029/2011JE003926.
- Schorghofer, N., Aharonson, O., 2014. The lunar thermal ice pump. *Astrophys. J.* 788 (169), 7. doi: 10.1088/0004-637X/788/2/169.
- Shkuratov, Y.G., Kreslavsky, M.A., Ovcharenko, A.A., et al., 1999. Opposition effect from Clementine data and mechanisms of backscatter. *Icarus* 141, 132–155. doi: 10.1006/icar.1999.6154.
- Smith, W.H.F., Wessel, P., 1990. Gridding with continuous curvature splines in tension. *Geophysics* 55, 293–305.
- Smith, D.E., Zuber, M.T., Neumann, G.A., et al., 1997. Topography of the Moon from the Clementine lidar. *J. Geophys. Res.* 102, 1591–1611. doi: 10.1029/96JE02940.
- Smith, D.E., Zuber, M.T., Jackson, G.B., et al., 2010. The lunar orbiter laser altimeter investigation on the lunar reconnaissance orbiter mission. *Space Sci. Rev.* 150, 209–241. doi: 10.1007/s11214-009-9512-y.
- Smith, D.E., Neumann, G.A., Jha, K., et al., LOLA PDS Archive, NASA Planetary Data System.
- Sori, M.M., Zuber, M.T., Head, J.W., et al., 2016. Gravitational search for cryptovolcanism on the moon: Constraints on early igneous activity. *Icarus*, 273, pp. 284–295. doi: 10.1016/j.icarus.2016.02.009.
- Speyerer, E.J., Robinson, M.S., 2013. Persistently illuminated regions at the lunar poles: Ideal sites for future exploration. *Icarus* 222, 122–136. doi: 10.1016/j.icarus.2012.10.010.
- Spudis, P.D., Bussey, D.B.J., Baloga, S.M., et al., 2013. Evidence for water ice on the Moon: Results for anomalous polar craters from the LRO Mini-RF imaging radar. *J. Geophys. Res.* 118, 2016–2029. doi: 10.1002/jgre.20156.
- Steinbrügge, G., Stark, A., Hussmann, H., et al., 2015. Measuring tidal deformations by laser altimetry. A performance model for the Ganymede laser altimeter. *Planet Space Sci.* 117. doi: 10.1016/j.pss.2015.06.013.
- Sunshine, J.M., Farnham, T.L., Feaga, L.M., et al., 2009. Temporal and spatial variability of lunar hydration as observed by the deep impact spacecraft. *Science* 326, 565–568. doi: 10.1126/science.1179788.
- Turcotte, D.L., 1987. A fractal interpretation of topography and geoid spectra on the Earth, Moon, Venus and Mars. *J. Geophys. Res.* 92, E597–E601.
- Tye, A.R., Fassett, C.I., Head III, J.W., et al., 2015. The age of lunar south circumpolar craters Haworth, Shoemaker, Faustini, and Shackleton: Implications for regional geology, surface processes, and volatile sequestration. *Icarus* 255, 70–77. doi: 10.1016/j.icarus.2015.03.016.
- Vondrak, R., Keller, J., Chin, G., et al., 2010. Lunar Reconnaissance Orbiter (LRO): Observations for lunar exploration and science. *Space Sci. Rev.* 150, 7–22. doi: 10.1007/s11214-010-9631-5.
- Wagner, R.V., Nelson, D.M., Plescia, J.B., et al., 2016. Coordinates of anthropogenic features on the Moon. *Icarus* doi: 10.1016/j.icarus.2016.05.011.
- Watson, K., Murray, B.C., Brown, H., 1961. The behavior of volatiles on the lunar surface. *J. Geophys. Res.* 66, 3033–3045.
- Whitten, J., Head III, J.W., Staid, M.I., et al., 2011. Lunar mare deposits associated with the Orientale impact basin: New insights into mineralogy, history, mode of emplacement, and relation to Orientale Basin evolution from Moon Mineralogy Mapper (M3) data from Chandrayaan-1. *J. Geophys. Res.* 116, E00G09. doi: 10.1029/2010JE003736.
- Whitten, J.L., Head III, J.W., 2013. Detecting volcanic resurfacing of heavily cratered terrain: Flooding simulations on the Moon using Lunar Orbiter Laser Altimeter (LOLA) data. *Planet Space Sci.* 85, 24–37. doi: 10.1016/j.pss.2013.05.013.
- Whitten, J.L., Head III, J.W., 2015a. Lunar cryptomaria: Physical characteristics, distribution, and implications for ancient volcanism. *Icarus* 247, 150–171. doi: 10.1016/j.icarus.2014.09.031.
- Whitten, J.L., Head III, J.W., 2015b. Lunar cryptomaria: Mineralogy and composition of ancient volcanic deposits. *Planet Space Sci.* 106, 67–81. doi: 10.1016/j.pss.2014.11.027.

- Wieczorek, M.A., Jolliff, B.L., Khan, A., et al., 2006. The constitution and structure of the lunar interior. *Rev. Mineral. Geochem.* 60, 221–364. doi:[10.2138/rmg.2006.60.3](https://doi.org/10.2138/rmg.2006.60.3).
- Wilhelms, D., 1987. Geologic History of the Moon, US Geological Survey Professional Paper 1348.
- Williams, J.G., Boggs, D.H., Folkner, W.M., 2008. DE421 Lunar Orbit, Physical Librations, and Surface Coordinates Rep. IOM 335-JW,DB,WF-20080314-001. Jet Propulsion Laboratory, Pasadena, California.
- Williams, J.G., Turyshev, S.G., Folkner, W.M., 2011. Lunar Geophysics and Lunar Laser Ranging, Ground-based Geophysics on the Moon, p. 3038.
- Williams, J.G., Boggs, D.H., Folkner, W.M., 2013. DE430 Lunar Orbit, Physical Librations, and Surface Coordinates, Rep. IOM 335-JW, DB,WF-20130722-016, Jet Propulsion Laboratory, Pasadena, California.
- Williams, J.G., Konopliv, A.S., Boggs, D.H., et al., 2014. Lunar interior properties from the GRAIL mission. *J. Geophys. Res.* 119, 1546–1578. doi:[10.1002/2013JE004559](https://doi.org/10.1002/2013JE004559).
- Yokota, Y., Matsunaga, T., Ohtake, M., et al., 2011. Lunar photometric properties at wavelengths 0.5–1.6 μm acquired by SELENE spectral profiler and their dependency on local albedo and latitudinal zones. *Icarus* 215, 639–660. doi:[10.1016/j.icarus.2011.07.028](https://doi.org/10.1016/j.icarus.2011.07.028).
- Zuber, M.T., Smith, D.E., Zellar, R., et al., 2010. The lunar reconnaissance orbiter laser ranging investigation. *Space Sci. Rev.* 150, 63–80. doi:[10.1007/s11214-009-9511-z](https://doi.org/10.1007/s11214-009-9511-z).
- Zuber, M.T., Head, J.W., Smith, D.E., et al., 2012. Constraints on the volatile distribution within Shackleton crater at the lunar South Pole. *Nature* 486, 378–381. doi:[10.1038/nature11216](https://doi.org/10.1038/nature11216).
- Zuber, M.T., Smith, D.E., Lehman, D.H., et al., 2013a. Gravity Recovery and Interior Laboratory (GRAIL): Mapping the lunar interior from crust to core. *Space Sci. Rev.* 178. doi:[10.1007/s11214-012-9952-7](https://doi.org/10.1007/s11214-012-9952-7).
- Zuber, M.T., Smith, D.E., Watkins, M.M., et al., 2013b. Gravity field of the Moon from the Gravity Recovery and Interior Laboratory (GRAIL) mission. *Science* 339. doi:[10.1126/science.1231507](https://doi.org/10.1126/science.1231507).